(4)

DIAGNOSTICS DEVELOPMENT FOR E-BEAM EXCITED AIR CHANNELS

Semiannual Technical Report No. 2

CONDUCTIVITY MEASUREMENTS IN AIR AFTERGLOWS

March 4, 1983

By: D. J. Eckstrom

Sponsored by:

DEFENSE ADVANCED RESEARCH PROJECTS AGENCY
1400 Wilson Blvd.
Arlington, VA 22209

Monitored by:

OFFICE OF NAVAL RESEARCH
800 North Quincy Street
Arlington, VA 22217

ARPA Order No. 4128
Contract No. N00014-81-C-0208
Effective Date: 15 January 1981
Expiration Date: 20 March 1983
Principal Investigator: D. J. Eckstrom (415) 859-4398

SRI Project PYU 2690
MP Report No. 83-035

SRI International
333 Ravenswood Avenue
Menlo Park, California 94025
(415) 326-6200
TWX: 910-373-2046
Telex: 334 486

SECURITY CLASSIFICATION OF THIS PAGE (When Data Entered)

REPORT DOCUMENTATION PAGE

READ INSTRUCTIONS BEFORE COMPLETING FORM

1. REPORT NUMBER	2. GOVT ACCESSION NO.	3. RECIPIENT'S CATALOG NUMBER
	AD-A125 997	

4. TITLE (and Subtitle)
DIAGNOSTICS DEVELOPMENT FOR E-BEAM EXCITED AIR CHANNELS. Conductivity Measurements in Air Afterglows

5. TYPE OF REPORT & PERIOD COVERED
Technical Report No. 2

6. PERFORMING ORG. REPORT NUMBER
MP Report 83-035

7. AUTHOR(s)
Donald J. Eckstrom

8. CONTRACT OR GRANT NUMBER(s)
N00014-81-C-0208

9. PERFORMING ORGANIZATION NAME AND ADDRESS
SRI International
333 Ravenswood Avenue
Menlo Park, CA 94025

10. PROGRAM ELEMENT, PROJECT, TASK AREA & WORK UNIT NUMBERS

11. CONTROLLING OFFICE NAME AND ADDRESS
Defense Advanced Research Projects Agency
1400 Wilson Boulevard
Arlington, VA 22209

12. REPORT DATE
8 March 1983

13. NUMBER OF PAGES
51

14. MONITORING AGENCY NAME & ADDRESS (if different from Controlling Office)
Office of Naval Research
800 North Quincy Street
Arlington, VA 22217

15. SECURITY CLASS. (of this report)
Unclassified

15a. DECLASSIFICATION/DOWNGRADING SCHEDULE

16. DISTRIBUTION STATEMENT (of this Report)
Approved for public release; distribution unlimited.

17. DISTRIBUTION STATEMENT (of the abstract entered in Block 20, if different from Report)

18. SUPPLEMENTARY NOTES

19. KEY WORDS (Continue on reverse side if necessary and identify by block number)
Charged particle beams, conductivity, microwave cavity perturbations, afterglows, electron density

20. ABSTRACT (Continue on reverse side if necessary and identify by block number)

Nonintrusive techniques for measuring conductivity decay in the afterglow air channel of a relativistic electron beam are reviewed, and the microwave cavity perturbation technique is found to offer adequate sensitivity. A right cylindrical cavity resonating in the TM_{010} mode at 1.5 GHz was fabricated, and a series of preliminary measurements in air was performed. The afterglow conductivity of laboratory air at 1 amagat is apparently dominated by ions. The conductivities of synthetic air at 10 torr at 250 to 1500 μs after the pulse

microseconds

cont

DD FORM 1 JAN 73 1473 EDITION OF 1 NOV 65 IS OBSOLETE

10 to the 8th power 5,000,000/cc

approx

are consistent with electron densities of 10^8 to $5 \times 10^6/cm^3$ and electron temperatures of ~ 0.15 eV. Surveys of conductivity histories at 5 pressures between 10 and 760 torr are also reported.

After the experimental set-up has been refined, conductivity studies in room temperature air will be repeated. Future work will include measurements on the ETA facility, measurements of shock-heated air, and measurements to investigate the field-induced detachment of negative ions in the afterglow.

ACKNOWLEDGMENTS

Dr. Tom Fessenden of Lawrence Livermore National Laboratory provided the suggestion and continuing encouragement to investigate the use of the microwave cavity perturbation technique for afterglow conductivity measurements. Dr. Robert M. Hill of our laboratory provided additional guidance and support in this work. Jay S. Dickinson assisted with the performance of the Febetron experiments. All of this assistance is gratefully acknowledged.

CONTENTS

ABSTRACT.....i
ACKNOWLEDGMENTS.....iii
LIST OF FIGURES.....v
LIST OF TABLES.....vi
I INTRODUCTION.....1
II ELECTROMAGNETIC PROPERTIES OF PLASMAS.....3
Complex Propagation Constants.....3
Sensitivity of Single Pass Measurements.....6
Multiple Pass Measurements.....11
III THE MICROWAVE RESONANT CAVITY TECHNIQUE.....12
Description.....12
Cavity Optimization.....17
Sensitivity of the Technique.....20
IV PRELIMINARY EXPERIMENTS.....24
Test Set-Up.....24
Conductivities at 760 and 10 torr.....28
Pressure Scans.....39
V CONCLUSIONS AND PLANS.....49

REFERENCES.....51

FIGURES

1. Effective Collision Frequencies in Air at 1 amagat.....9
2. Fringe Shift Due to Electrons in a Lossy Plasma.....10
3. Attenuation Due to Electrons in a Lossy Plasma.....12
4. Partial Mode Chart for Right Cylindrical Microwave Cavity.....14
5. Overlap Function for 1-cm-Diameter Plasma in Resonant Cavity.....18
6. Frequency Shift Due to 1-cm-Diameter Plasma in TM_{010} Mode of Cavity at λ = 19.2 cm.....21
7. Q Shift Due to 1-cm-Diameter Plasma in the TM_{010} Mode of Cavity at λ = 19.2 cm.....22
8. Preliminary Test Set-up.....25
9. Conductivity Measurement Setup Using Febetron.....26
10. Cavity Transmission for 30-torr Synthetic Air Using Frequency Modulation Technique.....27
11. Cavity Transmission Histories for 1 amagat Humid Air.....29
12. Transmission Profiles in Humid Air at 1 amagat.....31
13. Real Conductivity Histories for 1 amagat Humid Air.....32
14. Imaginary Conductivity History for 1 amagat Humid Air.....33
15. Collision Frequencies Deduced for Charged Particles in Air Afterglows.....34
16. Deduced Electron Density Histories for 1 amagat Humid Air.....35
17. Reduced Ion Density History for 1 amagat Humid Air.....38
18. Cavity Transmission Histories for 10 torr Synthetic Air.....40
19. Transmission Profiles in Synthetic Air at 10 torr.....41
20. Real Conductivity Histories for 10 torr Synthetic Air.....42
21. Electron Density Histories for 10 torr Synthetic Air.....43
22. Cavity Transmission Histories for Synthetic and Laboratory Air.....45
23. Conductivity Histories in Synthetic Air for Various Pressures.....47
24. Conductivity Histories in Synthetic Air for Various Pressures.....48

TABLES

1. Complex Conductivities in Special Cases.....7
2. Complex Refractive Indices in Special Cases.....8

I INTRODUCTION

The propagation of a high current relativistic electron beam through a gaseous medium is strongly influenced by the conductivity of the medium. For an initial beam pulse into air, the conductivity is generated by collisional ionization of the air by primary beam electrons and by the numerically dominant cascade or secondary electrons; if the beam-generated inductive electric fields are strong enough, additional ionization is created by the field-driven secondary electrons. For typical beam parameters into atmospheric density (1 amagat) air, electron densities in the beam channel are on the order of $10^{16}/cm^3$, which corresponds to a conductivity (assuming $T_e \gtrsim 300$ K) of order $\sigma \approx 10^{13}/s$ (units of equal conductivity are $9 \times 10^9\ s^{-1} = 1$ mho-$m^{-1} = 10^{-2}$ mho-cm^{-1}).

When multiple beam pulses are fired in a sequence, the residual conductivity in the afterglow air channel from previous pulses can become large enough to influence the propagation of a subsequent pulse. The critical value is of order $\sigma \simeq 3 \times 10^9\ s^{-1}$, which corresponds to room temperature electron densities $n_e \simeq 10^{12}/cm^3$. Beams of interest will be approximately 1 cm in diameter.

The objective of the work described here is to develop and demonstrate a diagnostic technique capable of measuring conductivity levels of $\sigma \lesssim 3 \times 10^{-9}\ s^{-1}$ in a 1-cm-diameter plasma. Since physical probes would most likely perturb the beam, and would be subject to damage as well, the techniques considered must be nonintrusive, which means that they will involve the interaction of the plasma with a diagnostic eletromagnetic wave or field.

We first describe that interaction for EM waves propagated through the plasma, and we show sensitivity limits for this approach (i.e., classical interferometry and absorptivity in the infrared through microwave frequency ranges). After showing that such single-pass measurement techniques are inadequate, we then consider a multiple-pass or standing wave technique, namely, a microwave cavity resonance perturbation technique, which is well suited for these measurements. Optimization of the cavity design and anticipated performance characteristics of the system are then described.

The resulting measurement system has been used to perform several preliminary checkout measurements of the conductivity in the afterglow of air excited by a Febetron 706 electron beam. These measurements give first results for room temperature laboratory and synthetic air over the pressure range from 10 to 760 torr. As these measurements are refined, they will provide benchmarks for calculating the afterglow plasma properties using air chemistry codes. Air chemistry is sufficiently complex to necessitate such comparisons at room temperature, and even more difficult at the elevated temperatures characteristic of heated channels. We plan to address this problem in the future by making measurements in shock-heated air.

When electron and ion densities are anywhere near comparable magnitudes, the plasma properties are dominated by the electrons. However, in a medium where electron attachment rates are large compared with electron-positive ion recombination rates, negative ion densities can be orders of magnitude higher than electron densities in the late afterglow. This might be the case for room temperature air at atmospheric pressure, and we find anomalies in our 1 amagat data that suggest a role of negative ions. While this is of interest of itself, it also illustrates the possibility that the conductivity could rapidly change when fields from a propagating pulse interact with the afterglow plasma. It may be possible to simulate this effect in our experiments by applying a short pulsed field, either DC or microwave, to the afterglow plasma in the cavity and measuring the resulting charge in conductivity.

II ELECTROMAGNETIC PROPERTIES OF PLASMAS

This subject is a large and complicated one, which easily occupies entire books. A particularly useful source relevant to diagnostics of plasmas is the book by Heald and Wharton, Plasma Diagnostics with Microwaves [HW65]. Here we will summarize the relevant equations required in our analyses.

Complex Propagation Constants

The scalar dielectric constant of a linear isotropic medium, κ, is the ratio of permittivities of a medium to vacuum:

$$\kappa = \varepsilon/\varepsilon_o \quad , \tag{2.1}$$

while the scalar conductivity of such a medium, σ, is

$$\vec{J} = \sigma\vec{E} \quad . \tag{2.2}$$

These two parameters can be combined to form a complex dielectric constant, $\bar{\kappa}$, as

$$\bar{\kappa} \equiv \kappa_r - j\kappa_i = \kappa - j\sigma/\omega\varepsilon_o \quad , \tag{2.3}$$

where $j = \sqrt{-1}$. Likewise, one can define a complex conductivity, $\bar{\sigma}$:

$$\bar{\sigma} \equiv \sigma_r + j\sigma_i = \sigma + j\omega(\kappa - 1)\varepsilon_o \quad . \tag{2.4}$$

Comparison of the two expressions shows that they are related by

$$\bar{\kappa} = \kappa_r - j\kappa_i = 1 - j\frac{\bar{\sigma}}{\varepsilon_o\omega} = \left(1 + \frac{\sigma_i}{\varepsilon_o\omega}\right) - j\frac{\sigma_r}{\varepsilon_o\omega} \tag{2.5}$$

and

$$\bar{\sigma} = \sigma_r + j\sigma_i = j\varepsilon_o\omega(\bar{\kappa} - 1) = \kappa_i\varepsilon_o\omega + j(\kappa_r - 1_o)\varepsilon\ \omega \quad . \tag{2.6}$$

Since κ_i is related to dissipation, it is common in microwave measurements to refer to the "loss factor" = $\kappa_i = \sigma_r/\varepsilon_o\omega$. Further, the "loss tangent" is defined as

$$\tan \delta = \frac{\kappa_i}{\kappa_r} = \frac{\sigma_r}{\varepsilon_o \omega \kappa} \quad . \tag{2.7}$$

Propagation of an EM wave in a plasma can conveniently be described in terms of a complex refractive index, $\bar{\mu}$, which is related to the complex dielectric constant by

$$\bar{\mu} = \mu - j\chi = \bar{\kappa}^{1/2} \quad . \tag{2.8}$$

The fringe shift, ΔS, is related to the change in the real part of the index as

$$\Delta S = (\mu_o - \mu)/\lambda \quad \text{cm}^{-1} \quad , \tag{2.9}$$

while the attenuation of a probe beam is

$$\alpha = \chi\omega/c \quad \text{cm}^{-1} \quad . \tag{2.10}$$

In terms of the complex conductivity, the refractive indices can be written as

$$\left\{ \begin{matrix} \mu \\ \chi \end{matrix} \right\} = \frac{1}{\sqrt{2}} \left\{ \pm \left(1 + \frac{\sigma_i}{\varepsilon_o \omega} \right) + 1 \left[\left(+ \frac{\sigma_i}{\varepsilon_o \omega} \right)^2 + \left(\frac{\sigma_r}{\varepsilon_o \omega} \right)^2 \right]^{1/2} \right\}^{1/2} \quad . \tag{2.11}$$

Although the parameters described above are usually presented as approximations in one limit or another (D.C., $\omega \ll \nu$; A.C., $\omega \gg \nu$; ν = constant), all of the parameters can be given in complete generality through the expression for complex conductivity in terms of the momentum transfer collision frequency $\nu(v)$ and the electron velocity distribution function $f_o(v)$ as [HW65]

$$\bar{\sigma} = - \frac{4\pi}{3} \frac{ne^2}{m} \int_o^\infty \frac{1}{\nu + j\omega} \frac{df_o(v)}{dv} v^3 dv \quad . \tag{2.12}$$

This expression can be put in more familiar form by defining a new complex function, namely, a complex collision frequency $\bar{\nu} \equiv \nu_r + j\nu_i$. This function can be defined in terms of the integral in equation (2.12) for arbitrary electron distribution functions, but when the distribution is Maxwellian, it becomes explicitly

$$\bar{\nu} \equiv \frac{8}{3\sqrt{\pi}} \left(\frac{m}{2kT}\right)^{5/2} \int_0^\infty \frac{\nu + j\omega}{1 + \nu^2/\omega^2} v^4 \exp\left(\frac{-mv^2}{2kT}\right) dv \quad . \tag{2.13}$$

This parameter can be calculated for any gas (or gas mixture) for which $\nu(v)$ is known. Then, by introducing in addition the plasma frequency, ω_p, where

$$\omega_p^2 = \frac{n_e e^2}{m_e \varepsilon_o} \quad , \tag{2.14}$$

the real and imaginary conductivities can be written simply as

$$\frac{\sigma_r}{\varepsilon_o \omega} = \frac{\nu_r}{\omega} \frac{\omega_p^2}{\omega^2} \tag{2.15}$$

$$\frac{\sigma_i}{\varepsilon_o \omega} = -\frac{\nu_i}{\omega} \frac{\omega_p^2}{\omega^2} \quad . \tag{2.16}$$

Note again that this description of the conductivity is completely general, applying to arbitrary values of ω_p, ω, and ν. It is not even necessary that the electron distribution function be Maxwellian; but it must be known if equation (2.12) is to be evaluated. However, it is cumbersome to re-evaluate the integral in equation (2.13) for each combination of ω and ν, so it is worth examining some special cases. First, when $\omega << \nu$ (the D.C. limit),

$$\frac{\nu + j\omega}{1 + \nu^2/\omega^2} \rightarrow \frac{\omega^2}{\nu} + j\frac{\omega^3}{\nu^2} \quad . \tag{2.17}$$

When $\omega >> \nu$ (the A.C. limit),

$$\frac{\nu + j\omega}{1 + \nu^2/\omega^2} \rightarrow \nu + j\omega \quad . \tag{2.18}$$

We will therefore define $(\bar{\nu}_{eff})_{DC}$, $\langle \nu_{eff} \rangle_{AC}$, and $(\nu_{eff}^2)_{DC}$, as follows:

$$\frac{1}{(\bar{\nu}_{eff})_{DC}} = \frac{8}{3\sqrt{\pi}} \left(\frac{m}{2kT}\right)^{5/2} \int_0^\infty \frac{1}{\nu} v^4 \exp\left(\frac{-mv^2}{2kT}\right) dv \tag{2.19}$$

$$\langle \nu_{eff} \rangle_{AC} = \frac{8}{3\sqrt{\pi}} \left(\frac{m}{2kT}\right)^{5/2} \int_0^\infty \nu\, v^4 \exp\left(\frac{-mv^2}{2kT}\right) dv \tag{2.20}$$

$$\frac{1}{(\nu_{eff}^2)_{DC}} = \frac{8}{3\sqrt{\pi}} \left(\frac{m}{2kT}\right)^{5/2} \int \frac{1}{\nu^2} v^4 \exp\left(\frac{-mv^2}{2kT}\right) dv \; . \tag{2.21}$$

The effective collision frequencies in equations (2.19) and (2.20) were discussed by Heald and Wharton [HW65], and have been evaluated for several common molecular gases by Itikawa [It71,It73]. We introduce the third definition to write the simplified forms of the real and imaginary conductivities in Table 1. These effective collision frequencies are only a function of electron temperature. Itikawa's results can be used to calculate values for dry air (80% N_2, 20% O_2) or 50% humid air (add 8.5 torr H_2O), with the results shown in Figure 1. The values at the A.C. and D.C. limits are generally within 50% of each other, suggesting (but not proving) that use of an average value over the entire frequency range is not a bad approximation.

For completeness, we can substitute the expressions from Table 1 into equation (2.11) to arrive at limits for the real and imaginary refractive indices. These limits are given in Table 2.

Sensitivity of Simple Pass Measurements

To evaluate the sensitivity of single-pass probe experiments, particularly in the far-infrared and millimeter wavelength ranges, we have calculated the indices of refraction using the ν = constant expressions of Table 2 and the $(\bar{\nu}_{eff})_{DC}$ values for T_e = 300 K (0.025 eV) from Figure 1. The resulting ΔS and α values are plotted versus probe wavelength in Figures 2

Table 1

COMPLEX CONDUCTIVITIES IN SPECIAL CASES

Limit	σ_r	σ_i
D.C. ($\omega \ll \nu$)	$\sigma_r \rightarrow \frac{\varepsilon_o \omega_p^2}{(\bar{\nu}_{eff})_{DC}}$	$\sigma_i \rightarrow -\frac{\varepsilon_o \omega \omega_p^2}{(\nu_{eff}^2)_{DC}}$
A.C. ($\omega \gg \nu$)	$\sigma_r \rightarrow \frac{\varepsilon_o \omega_p^2}{\omega^2} \langle \nu_{eff} \rangle_{AC}$	$\sigma_i \rightarrow -\frac{\varepsilon_o \omega_p^2}{\omega}$
ν = constant	$\sigma_r \rightarrow \frac{\varepsilon_o \omega_p^2 \nu}{\omega^2 + \nu^2}$	$\sigma_i \rightarrow -\frac{\varepsilon_o \omega_p^2 \omega}{\omega^2 + \nu^2}$

Table 2

COMPLEX REFRACTIVE INDICES IN SPECIAL CASES

ν = constant

$$\left\{ \begin{matrix} \mu \\ \chi \end{matrix} \right\} = \frac{1}{\sqrt{2}} \left\{ \pm \left(1 - \frac{\omega_p^2}{\omega^2+\nu^2} \right) + \left[\left(1 - \frac{\omega_p^2}{\omega^2+\nu^2} \right)^2 + \left(\frac{\omega_p^2}{\omega^2+\nu^2} \frac{\nu}{\omega} \right)^2 \right]^{1/2} \right\}^{1/2}$$

$\omega << \nu$ (D.C.)

$$\left\{ \begin{matrix} \mu \\ \chi \end{matrix} \right\} = \frac{1}{\sqrt{2}} \pm \left\{ 1 \left(- \frac{\omega_p^2}{\left(\nu^2_{eff} \right)_{DC}} \right) + \left[1 \left(- \frac{\omega_p^2}{\left(\nu^2_{eff} \right)_{DC}} \right)^2 + \left(\frac{\omega_p^2}{\left(\bar{\nu}_{eff} \right)_{DC} \omega} \right)^2 \right]^{1/2} \right\}^{1/2}$$

$\omega >> \nu$ (A.C.)

$$\left\{ \begin{matrix} \mu \\ \chi \end{matrix} \right\} = \frac{1}{\sqrt{2}} \left\{ \pm \left(1 - \frac{\omega_p^2}{\omega^2} \right) + \left[\left(1 - \frac{\omega_p^2}{\omega^2} \right)^2 + \left(\frac{\langle \nu_{eff} \rangle_{AC}}{\omega} \frac{\omega_p^2}{\omega^2} \right)^2 \right]^{1/2} \right\}^{1/2}$$

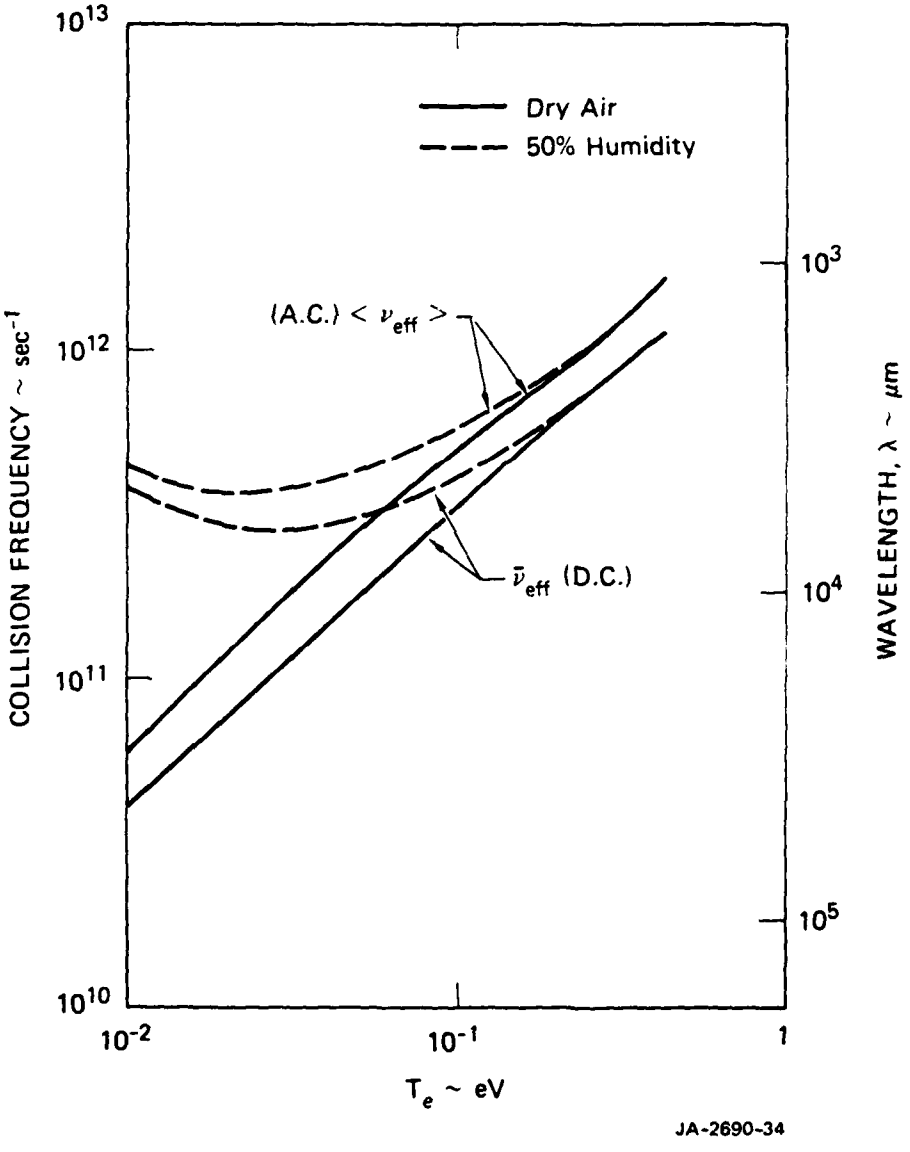

FIGURE 1 EFFECTIVE COLLISION FREQUENCIES IN AIR AT 1 amagat
[From Y. Itikawa, Phys. Fluids 16, 831 (1973)]

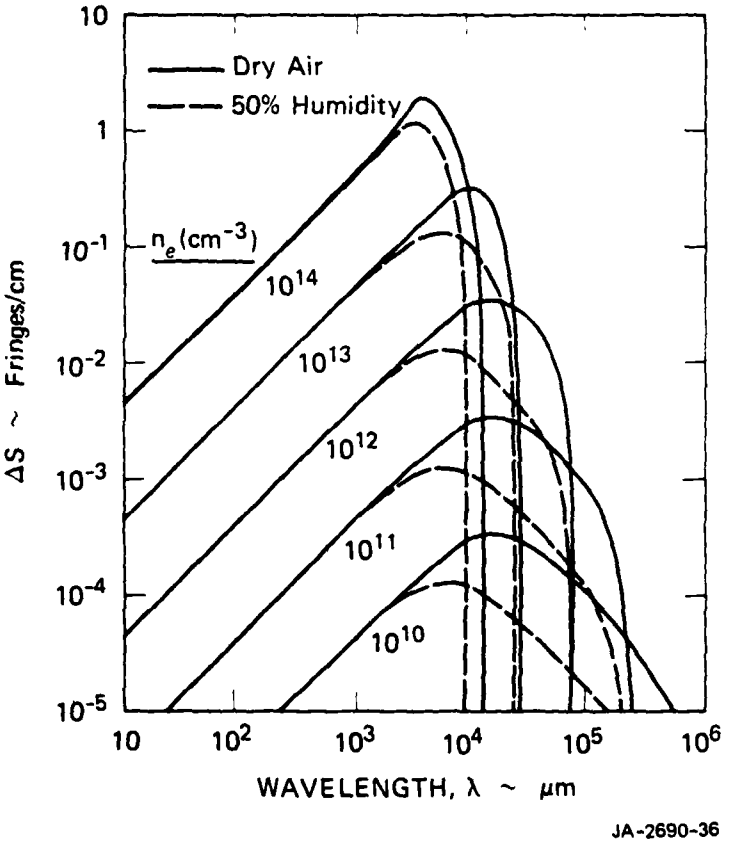

FIGURE 2 FRINGE SHIFT DUE TO ELECTRONS IN A LOSSY PLASMA
(1 amagat, T_e = 300°K)

and 3 for dry and 50% humid air at 1 amagat. In the A.C. limit (short wavelength), ΔS and α increase with λ and λ^2, respectively, and one tends to assume that sensitivity can be increased by increasing the wavelength indefinitely; however, this is clearly not the case: both ΔS and α reach a maximum when $\omega \approx \nu$, and subsequent increases in λ decrease the sensitivity.

If one assumes sensitivity limits of, say, a 1% change in measured intensity for a 1-cm-diameter plasma at 1 amagat, then $\alpha_{min} = 10^{-2}/cm$ and $\Delta S_{min} \approx 1.6 \times 10^{-3}/cm$. These limits correspond to $n_e \approx 10^{11}/cm^3$ in both cases. In fact, the sensitivity is not likely to be this good, since probe beam diameters will be about the same size as the plasma diamter, leading to strong deleterious refraction effects [KW64, Ves75, Ver79, DK75, GF71, Sh61]. Thus, a practical sensitivity limit for a single pass measurement is about $n_e = 10^{12}/cm^3$ at 1 amagat. Fringe shift measurements can be more sensitive at lower densities since the turnover due to terms in ν occurs at longer wavelengths, but the attenuation is proportional to ν, and so it becomes less sensitive. Note that in the range of maximum sensitivity, both α and ΔS are functions of both σ_i and σ_r, equation (2.11), so it is necessary to measure both α and ΔS to determine either σ_i or σ_r.

Multiple Pass Measurements

Greater sensitivity can be achieved by increasing the interaction pathlength between the probe beam and the plasma, in this case by probing with multiple passes through the plasma. At optical through millimeter wavelengths, this would be accomplished, for example, by switching from a single pass Mach-Zehnder interferometer to a multiple pass Fabry-Perot interferometer. However, such an approach is not entirely satisfactory, since the response of the transmission of a Fabry-Perot interferometer to an absorption is highly nonlinear, and since refraction effects still outweigh interference or absorption effects. At microwave frequencies, multiple pass sensitivity is achieved by using a cavity that completely contains the fields, thus eliminating refraction effects. Furthermore, the response of the cavity to perturbations is well defined. We devote the remainder of this report to the microwave cavity approach.

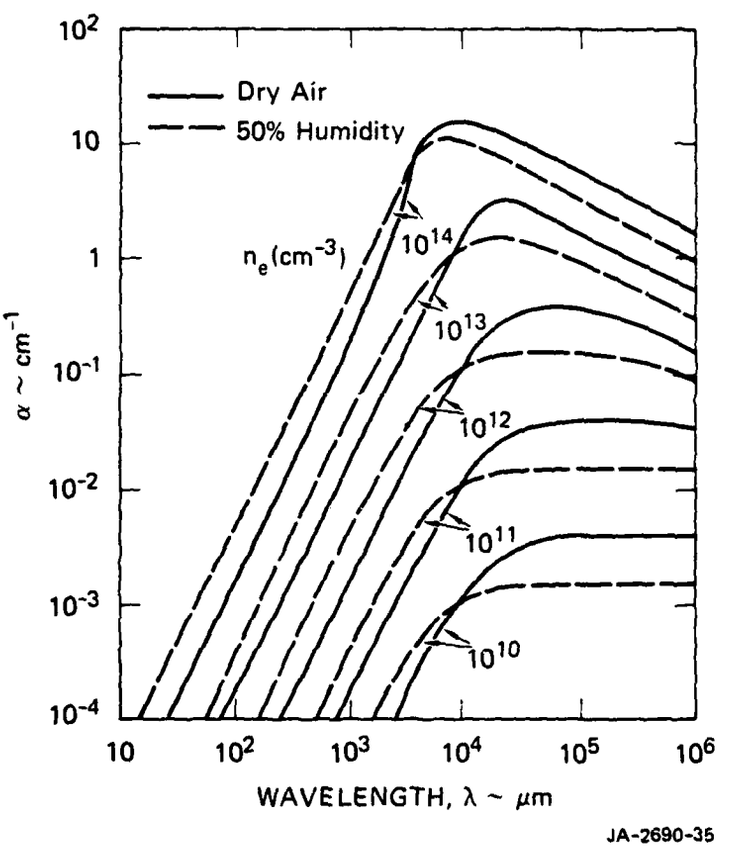

FIGURE 3 ATTENUATION DUE TO ELECTRONS IN A LOSSY PLASMA
(1 amagat, T_e = 300°K)

III THE MICROWAVE RESONANT CAVITY TECHNIQUE

Description

The properties of microwave cavities are described in several books, including Montomery's Technique of Microwave Measurements [Mo47]. Basically, a cavity supports transverse electric (TE) and transverse magnetic (TM) modes, each with a large number of resonant frequencies. For a right cylindrical cavity, the modes are further characterized by the subscripts "ℓmn," where ℓ is the number of standing waves in the azimuthal direction, m is the number of half waves in the radial direction, and n is the number of half waves in the axial direction. The resonant wavelengths are

$$\lambda = \frac{2}{\left[\left(\frac{2\chi_{\ell m}}{\pi D}\right)^2 + \left(\frac{n}{L}\right)^2\right]^{1/2}} \qquad (3.1)$$

where the $\chi_{\ell m}$ are the m'th roots of the Bessel functions $J_\ell(\chi)$. A few of the lowest mode frequencies are shown in Figure 4. Each of these resonances has an intrinsic unloaded cavity $Q = Q_u$, where Q is defined as 2π x the ratio of energy stored to the energy loss per cycle of oscillation of the resonant standing wave (due to resistive losses of the surface currents in the cavity). Again, for right cylindrical cavities, Q_u is related to the skin depth δ by

$$Q_u \frac{\delta}{\chi} = \frac{(\chi_{\ell m}^2 + p^2 D^2/L^2)^{1/2}}{2\pi\,(1 + D/L)} \qquad (n > 0) \qquad (3.2)$$

$$= \frac{\chi_{\ell m}}{\pi(2 + D/L)} \qquad (n = 0) \qquad (3.3)$$

where $p = n\pi/2$. The skin depth is further related to the resistivity ρ as

$$\delta = \left(\frac{\lambda\rho}{120\,\pi^2\mu}\right)^{1/2} \text{cm} \quad . \qquad (3.4)$$

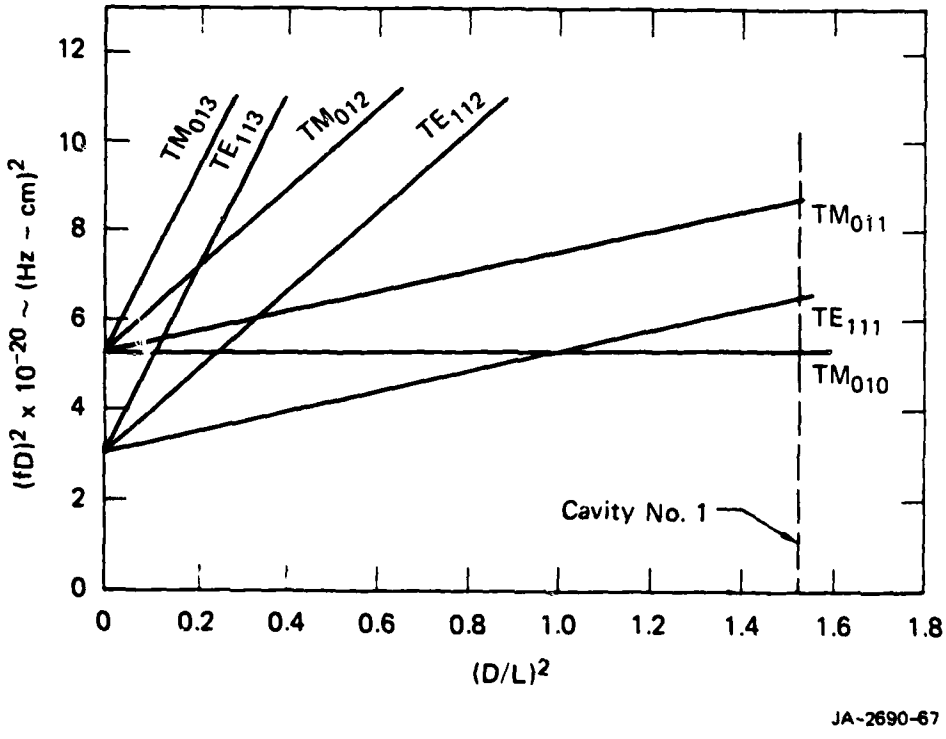

FIGURE 4 PARTIAL MODE CHART FOR RIGHT CYLINDRICAL MICROWAVE CAVITY

A high Q_u is achieved by choosing a cavity with high volume-to-surface ratio and by plating the interior surface with a low resistivity material like silver.

Both the resonant frequencies and the Qs of a cavity are perturbed by introducing a material with $\bar{\sigma} \neq \kappa_o$, where κ_o is the dielectric constant of air. Slater [S146] derived a perturbation formula as

$$\Delta\left(\frac{1}{Q}\right) - 2j\,\frac{\Delta\omega}{\omega} = \frac{1}{\varepsilon_o \omega}\,\frac{\int_v \vec{J} \cdot \vec{E}\, dv}{\int_v \vec{E} \cdot \vec{E}_o\, dv} \,. \tag{3.5}$$

When the perturbation is small enough that the electric fields retain their initial values, $\vec{E} = \vec{E}_o$, the perturbation formula can be written

$$\Delta\left(\frac{1}{Q}\right) - 2j\,\frac{\Delta\omega}{\omega} = \frac{1}{\varepsilon_o \omega}\,\frac{\int_v \bar{\sigma}(r)\, E^2(r)\, dv}{\int_v E^2(r)\, dv} \tag{3.6}$$

$$\simeq \frac{\bar{\sigma}}{\varepsilon_o \omega}\,\frac{\int_{\text{plasma}} E^2(r)\, dv}{\int_{\text{cavity}} E^2(r)\, dv} \tag{3.7}$$

where we have now identified the perturbation as a plasma. The last expression shows clearly that <u>if the area of the plasma is known</u> so that the ratio of integrals can be evaluated, then the real and imaginary conductivities, σ_r and σ_i, can be determined by measuring $\Delta\left(\frac{1}{Q}\right)$ and $\Delta\omega/\omega$, respectively. This is in contrast to the single pass probe measurement, described in the previous section, where both ΔS and α had to be measured to determine σ_r or σ_i.

We emphasize again that in the resonant cavity perturbation technique, the change in cavity Q is directly proportional to σ_r, and, furthermore, if $\omega \ll \nu$, this gives the D.C. conductivity, $\sigma_r = \sigma_{D.C.}$. This is the parameter of primary interest in these measurements.

The Slater formula requires corrections when the perturbations become large. In our case, our right cylindrical cavity must have holes in the ends to pass the electron beam, and, in the Febetron experiments reported here, a

quartz tube was inserted the length of the cavity to confine the plasma to a known area. Corrections for such effects have been derived for $\Delta\omega/\omega$ versus σ_i. [Th63, Th65, Lu68], but apparently not for $\Delta(\frac{1}{Q})$ versus σ_r. Therefore, we base our results to date on the Slater formula, with the plan to calibrate the correction using liquids of known conductivity [BF49, SL46].

There are two ways to determine the $\Delta(1/Q)$ change due to a plasma perturbation. The first is to measure the cavity transmission at several frequencies in the vicinity of the resonance and to cross plot the power transmitted at finite time intervals following the e-beam pulse. Then, by definition, $Q(t) = f_o(t)/\Delta f(t)$. The second is based on the relative value of the transmission itself. For the empty cavity, the losses giving rise to the loaded Q_ℓ are

$$\frac{1}{Q_\ell} = \frac{1}{Q_u} + \frac{1}{Q_{output}} + \frac{1}{Q_{input}} \equiv \frac{1}{Q_u} + \frac{\beta_1}{Q_u} + \frac{\beta_2}{Q_u} = \frac{1}{Q_u} + \frac{1}{Q_{ext}} \qquad (3.8)$$

where β_1 and β_ℓ are defined in terms of the ratios of the coupling Qs to Q_u. The power transmission through the cavity is then [Ha63]

$$T_c = \frac{4\,\beta_1\beta_2}{(1+\beta_1+\beta_2)^2 + 4Q_u^2\left(\frac{\omega-\omega_r}{\omega_r}\right)^2} \qquad (3.9)$$

At the resonant frequency $\omega = \omega_r$, this simplifies to

$$T_c^o = (Q_\ell/Q_{ext})^2 \quad . \qquad (3.10)$$

When a plasma is introduced, the unloaded Q is perturbed by

$$\frac{1}{Q_u'} = \frac{1}{Q_u} + \Delta\left(\frac{1}{Q}\right) \qquad (3.11)$$

while the external Q stays constant

$$Q_{ext}' = Q_{ext} \quad . \tag{3.12}$$

It can be shown that the ratio of cavity transmissions with and without a plasma is then

$$\frac{T_c'}{T_c} = \frac{1 + 4Q_\ell^2 \left(\frac{\omega-\omega_r}{\omega_r}\right)^2}{\left(\frac{Q_\ell}{Q_\ell'}\right)^2 + 4Q_\ell^2 \left(\frac{\omega-\omega_r'}{\omega_r'}\right)^2} \quad . \tag{3.13}$$

If both measurements are done at the resonance peak, this becomes simply

$$\frac{T_c'}{T_c} = \left(\frac{Q_\ell'}{Q_\ell}\right)^2 \tag{3.14}$$

Thus, a measurement of the cavity transmission at the resonance peak suffices to give $\Delta(1/Q)(t)$ and therefore $\sigma_r(t)$.

Cavity Optimization

Maximum sensitivity to a centerline plasma is achieved by choosing a TM_{0M0} mode, for which the fields are

$$E_r = E_\theta = 0 \tag{3.15}$$

and

$$E_Z = J_o\left(\chi_{\ell m} r/R_c\right) \quad . \tag{3.16}$$

The overlap function, which is the ratio of integrals in equation (3.7), then has the values shown in Figure 5. While this figure suggests that maximum sensitivity is achieved by using a small radius cavity and a high order mode ($m > 3$), a more detailed look at cavity optimization is appropriate.

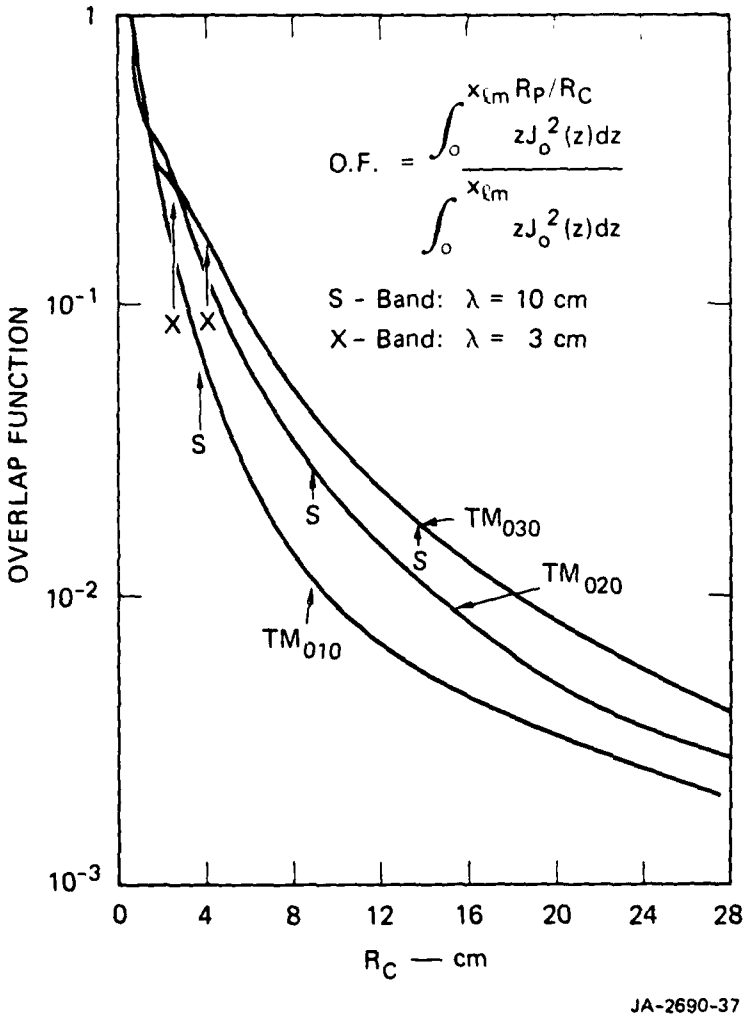

FIGURE 5 OVERLAP FUNCTION FOR 1-cm-diameter PLASMA IN RESONANT CAVITY

We begin the analysis with the equation for cavity transmission, equation (3.10). Taking the partial derivative, and using equation (3.11), yields

$$\frac{\partial T_c^{\,o}}{T_c^{\,o}} = -2Q_\ell \Delta\left(\frac{1}{Q}\right) \simeq -2Q_u \Delta\left(\frac{1}{Q}\right) \tag{3.17}$$

Optimization of the cavity now consists of maximizing the product of Q_u and $\Delta(1/Q)$. For a right cylindrical cavity with $TM_{\ell m0}$ modes, Q_u was given in equation (3.3). Since the skin depth, δ, is proportional to $\lambda^{1/2}$, $\delta = \delta_o \lambda^{1/2}$, the complete expression can be written

$$Q_u = \frac{\lambda}{\delta_o} \frac{\chi_{\ell m}}{\sqrt{\lambda}\ \ \pi(2 + D/L)} \quad . \tag{3.18}$$

To evaluate $\Delta(1/Q)$, we find that the overlap function can be approximated by

$$O.F. \simeq \frac{\pi}{2} \chi_{\ell m} \left(\frac{R_p}{R_c}\right)^2 \quad . \tag{3.19}$$

so that

$$\Delta\left(\frac{1}{Q}\right) = \frac{\sigma_r}{\varepsilon_o \omega} \frac{\pi}{2} \chi_{\ell m} \left(\frac{R_p}{R_c}\right)^2 \quad . \tag{3.20}$$

Combining equations (3.18) and (3.20) into (3.17) with the additional note that $\chi_{\ell m} = 2\pi R_c/\lambda$ yields the desired result

$$\frac{\partial T_c^{\,o}}{T_c^{\,o}} = \sigma_r \cdot \frac{2\pi^2}{\varepsilon_o \delta_o} \frac{R_p^{\,2}}{(2 + D/L)} \frac{1}{\sqrt{\lambda}} \quad . \tag{3.21}$$

We want a cavity that has the maximum $\partial T_c/T_c$ for a given σ_r and R_p. We see that the sensitivity is independent of the mode (within the $TM_{\ell m0}$ manifold) and the cavity diameter, and depends only on δ_o, D/L, and $\lambda^{1/2}$ (obviously, λ and mode determine the diameter). δ_o and D/L should be minimized to achieve maximum sensitivity; this maximizes Q_u, which is desirable as can readily be seen from equation (3.17).

We note that the wavelength dependence suggests as short a wavelength as possible. However, there are some limitations on reducing that parameter. Guidelines in the literature suggest that the length of the cavity be at least 4 times the hole diameter [SL46, Th63, Th65] and that the cavity radius be about 10 times the plasma diameter [Lu68]. Furthermore, λ should be greater than $\pi D_{aperture}$ to avoid radiation losses out the holes. Finally, D/L > 1 facilitates operation on the TM_{0m0} modes without interference from higher order modes.

We have chosen $D_{aperture}$ = 3 cm to accomodate electron beam passage without interference on ETA and ATA experiments. We have compromised on the above conflicting requirements by choosing L = 11.94 cm and D = 14.73 cm operating in the TM_{010} mode. The calculated resonance frequency in this case is 1.558 GHz, while the measured value is 1.5624 GHz (λ = 19.2 cm). The cavity was silver plated after assembly to minimize surface resistance. The calculated Q_u was 28,000 and the measured value is around 19,000. The cavity is fitted with two N-type vacuum feedthroughs with small loop antennas for coupling energy in and out. These loops have thus far been run with very small coupling coefficients, resulting in $Q_\ell \simeq 12{,}000$, for maximum sensitivity. In future experiments, the coupling can be increased to lower Q_ℓ to about 2500, which will allow measurements of 5 times higher conductivities if desired.

Sensitivity of the Technique

We have used equation (3.7) together with the ν = constant expressions for σ_r and σ_i from Table 1, the $(\bar{\nu}_{eff})_{DC}$ values for T_e = 300 K from Figure 1, and the cavity parameters given above to calculate $\Delta f/f$ and $\Delta(1/Q)$ for a 1-cm-diameter centerline plasma. The results are presented in Figures 6 and 7. Experience to date indicates that with the couplings adjusted for maximum Q_ℓ ($\simeq$ 12,000), we can detect frequency shifts of less than 100 kHz, which

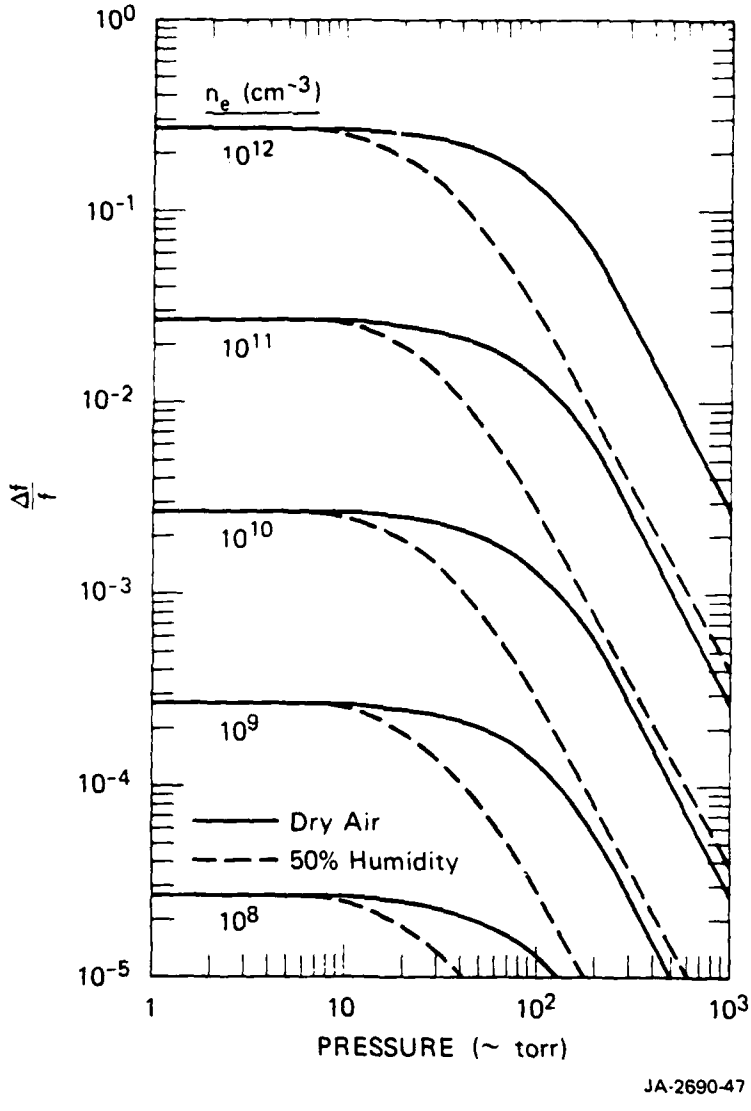

FIGURE 6 FREQUENCY SHIFT DUE TO 1-cm DIAMETER PLASMA IN TM_{010} MODE OF CAVITY AT λ = 19.2 cm ($T_g = T_e$ = 300 K, R_c = 7.36 cm)

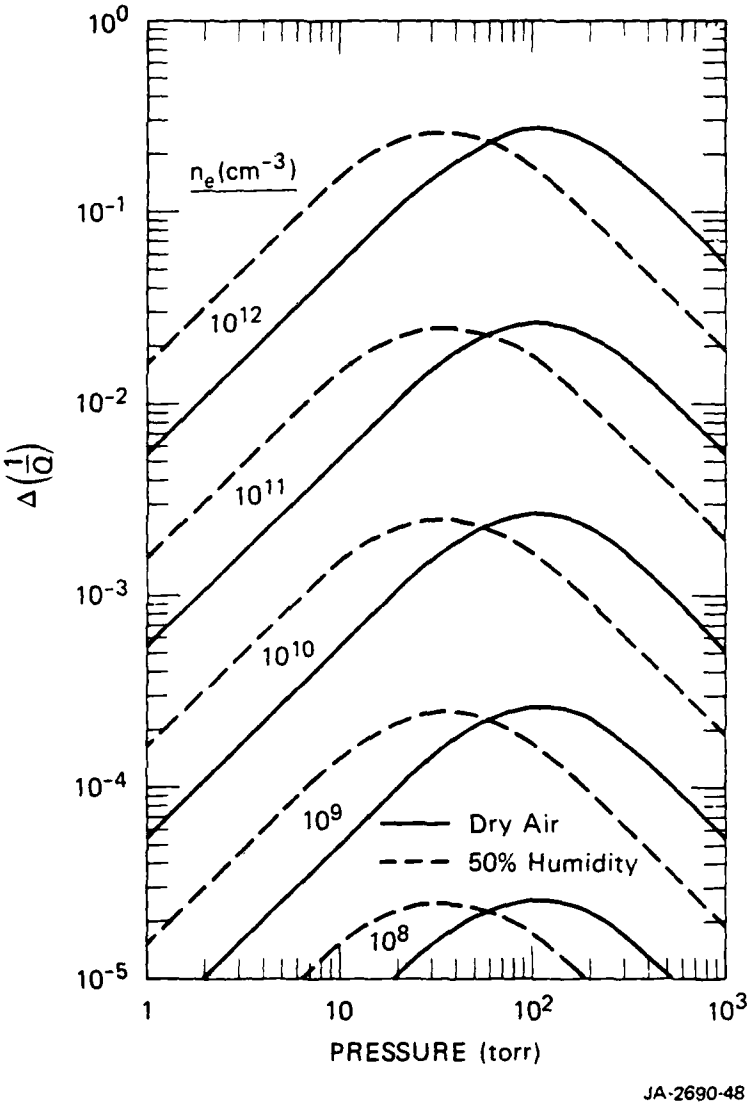

FIGURE 7 Q SHIFT DUE TO 1-cm DIAMETER PLASMA IN TM_{010} MODE OF CAVITY AT λ = 19.2 cm

($T_g = T_e$ = 300 K, R_c = 7.36 cm)

corresponds to $\Delta f/f < 6 \times 10^{-5}$. For the cold plasma conditions of Figure 6, this corresponds to electron densities of 10^{10} and $10^{11}/cm^3$ for 1 amagat of dry and humid air, respectively. Likewise, we can detect $\Delta(1/Q)$ changes as small as 5×10^{-6}, which corresponds to electron densities of order $10^{8}/cm^3$ at 1 amagat. Thus, the technique exceeds the sensitivity requirements of the task. (It becomes easier to operate the experiment with less sensitivity.)

IV PRELIMINARY EXPERIMENTS

Test Set-Up

The experimental layout for a set of experiments designed to check the technique and obtain preliminary data is shown schematically in Figure 8. The details of the attachment of the cavity to the Febetron 706 are shown in Figure 9. The Febetron beam is rather diffuse, and scattering is accentuated by the beam's passage through a second foil and hibatchi structure, so that an unconfined beam would occupy a large but unknown volume of the cavity. Therefore, we performed most of these experiments with a quartz tube, 26.5-mm ID by 30-mm OD lining the cavity, to confine and define the area of the plasma. This corresponds to a plasma area seven times that of a 1-cm-diameter plasma, and consequently the sensitivity limits in these experiments corresponds to electron densities one seventh of those quoted above.

The Q of the cavity was determined first, by using the sweep oscillator in the CF/ΔF mode, sweeping $\pm$ 1 MHz around the resonance frequency. The transmission of the cavity was displayed on an oscilloscope that had the x-axis input driven by the sweep output. It was possible to read the Δf of the transmission curve to about 10 kHz, giving the loaded cavity Q to $\sim$ 8% accuracy. The crystal detector used in these experiments (HP 423B) was nonlinear in the range of powers used, and it was necessary to correct these and other results for that effect.

We performed one experiment that provides a nice qualitative demonstration of the plasma perturbation technique. We used an external ramp function generator to frequency modulate the sweep oscillator at a modulation rate of 5 kHz and a modulation amplitude of $\pm$ 700 kHz around the resonance frequency. The transmission history for several modulation cycles with an empty cavity is shown in Figure 10(a). The transmission curves are distorted from the normal Lorentzian shape by "cavity pulling effects," but the regularity and constant amplitude of the transmission peaks are clear. Figure 10(b) repeats the transmission history, but now the Febetron was fired into 30 torr of synthetic air in the cavity at t = 0. The first pulse in the train has T = 0 through the cavity, and the gradual recovery of peak transmission as the

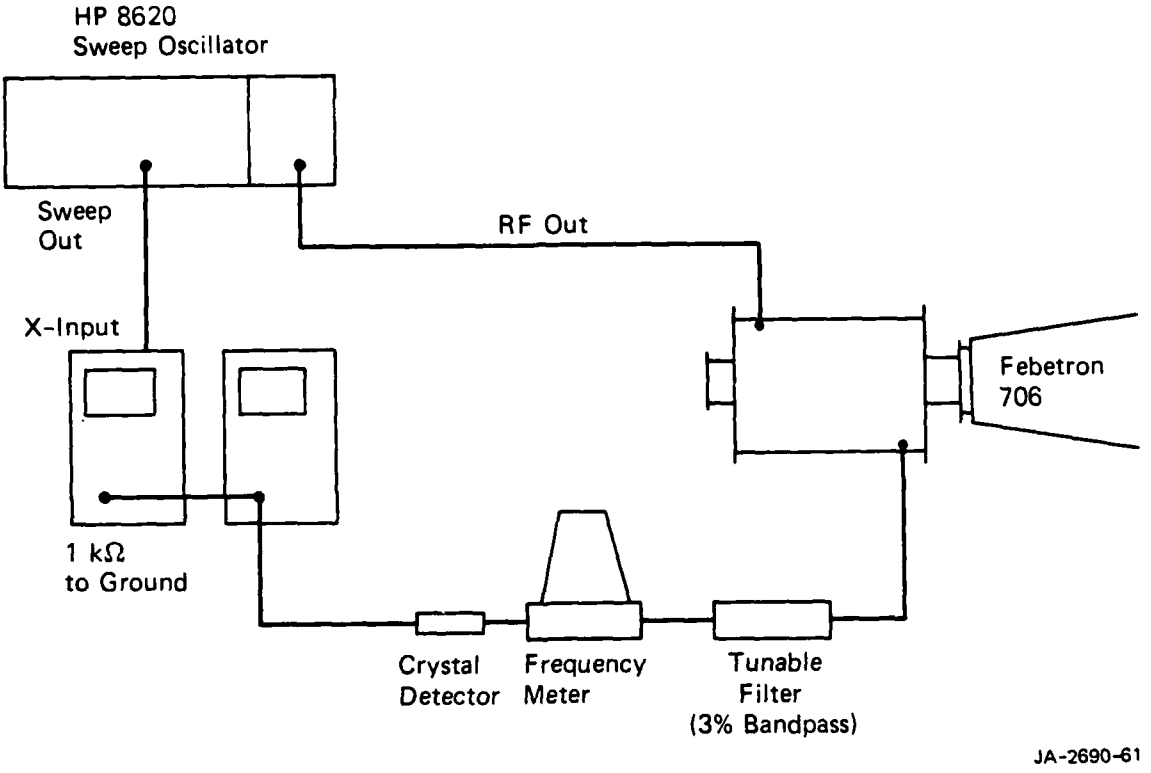

FIGURE 8 PRELIMINARY TEST SET-UP

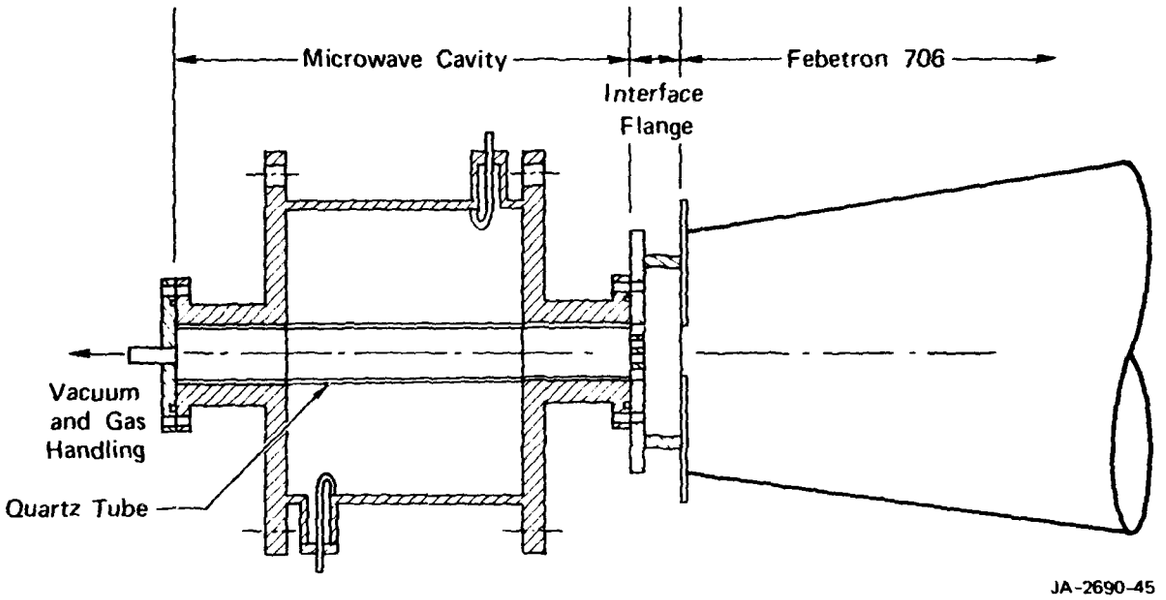

FIGURE 9 CONDUCTIVITY MEASUREMENT SETUP USING FEBETRON

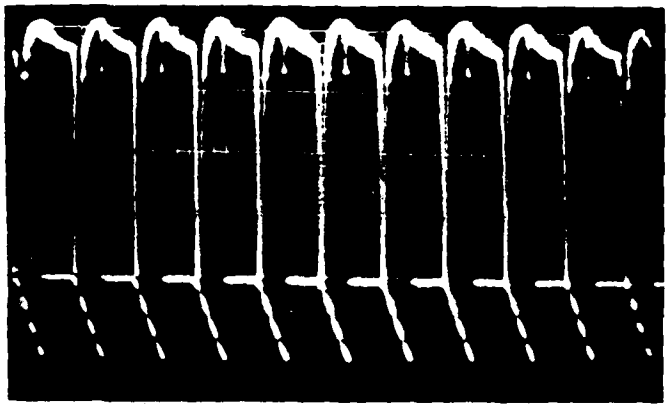

(a) No Febetron Pulse

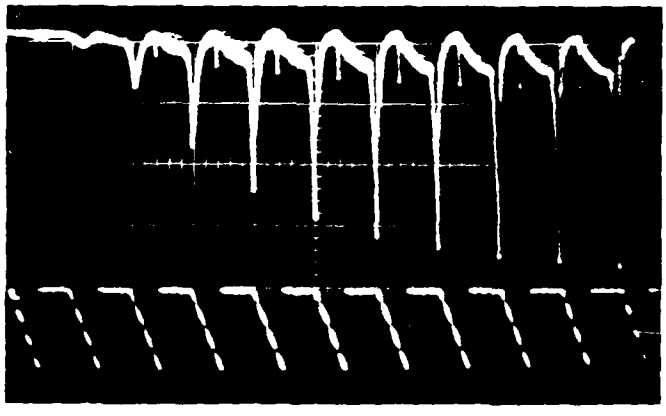

(b) Febetron Pulse at t = 0

JP-2690-54

FIGURE 10 CAVITY TRANSMISSION FOR 30 torr SYNTHETIC AIR USING FREQUENCY MODULATION TECHNIQUE

Upper Trace: Transmitted Power

Lower Trace: Frequency Modulation Voltage, Shifted So Start of Voltage Ramp Coincides With Peak of Unperturbed Cavity Transmission

plasma decays on a millisecond time scale is clearly seen. Also, the frequency shift of ~ 30 kHz of the second pulse and the smaller shift of the third pulse are clearly detectable. This technique could be a rapid way to accumulate data if the results could be displayed in a more accurate format and if the cavity pulling effects could be eliminated (perhaps by inserting an isolator in the line between the source and the cavity). However, it seems unlikely that the frequency modulation could be made fast enough to study an afterglow decay in full density air, which occurs in a few microseconds.

Conductivities at 760 and 10 torr

The normal technique for acquiring data was to switch the sweep oscillator to the cw mode and adjust the frequency to resonance, indicated by a signal amplitude corresponding to the peak of the transmission curve. A transmission history at that frequency was then acquired using a normal time base sweep triggered by the Febetron pulse. The source frequency was then adjusted to a number of + or - offset frequencies with the test repeated at each frequency. The sweep oscillator frequency could not be read accurately enough to set specific frequencies, so instead specific signal amplitudes were set ($T = 1/2T_{max}$, $1/4T_{max}$, etc.) and the frequencies were later inferred from the empty cavity transmission curve. This procedure is not satisfactory because of the uncertainty of the set frequency and because the cw frequency of this oscillator can drift over 100 kHz in a moment. Future experiments will require a frequency-stabilized source.

Representative tracings of oscillographs for such experiments in a cavity opened to humid laboratory air are presented in Figure 11. The scope was set up with zero transmission at the top of the figure and T_{max} producing nearly full-scale deflection as in the top trace. The signal amplitudes decrease as the frequency is tuned off resonance. The transmission goes to 0 at $t = 0$ (limited by instrument time constants), and then recovers to the initial value on a μs time scale. There are two significant features of these traces. First is the symmetry of the traces at + and - frequency offsets, indicating that the change in $\Delta(\frac{1}{Q})$ is large compared with $\Delta f/f$, as expected at 1 amagat (see Figures 6 and 7). The second feature is the ringing of the transmission at a frequency that is at least approximately equal to the preset offset frequency. Understanding and eliminating this effect will require further work.

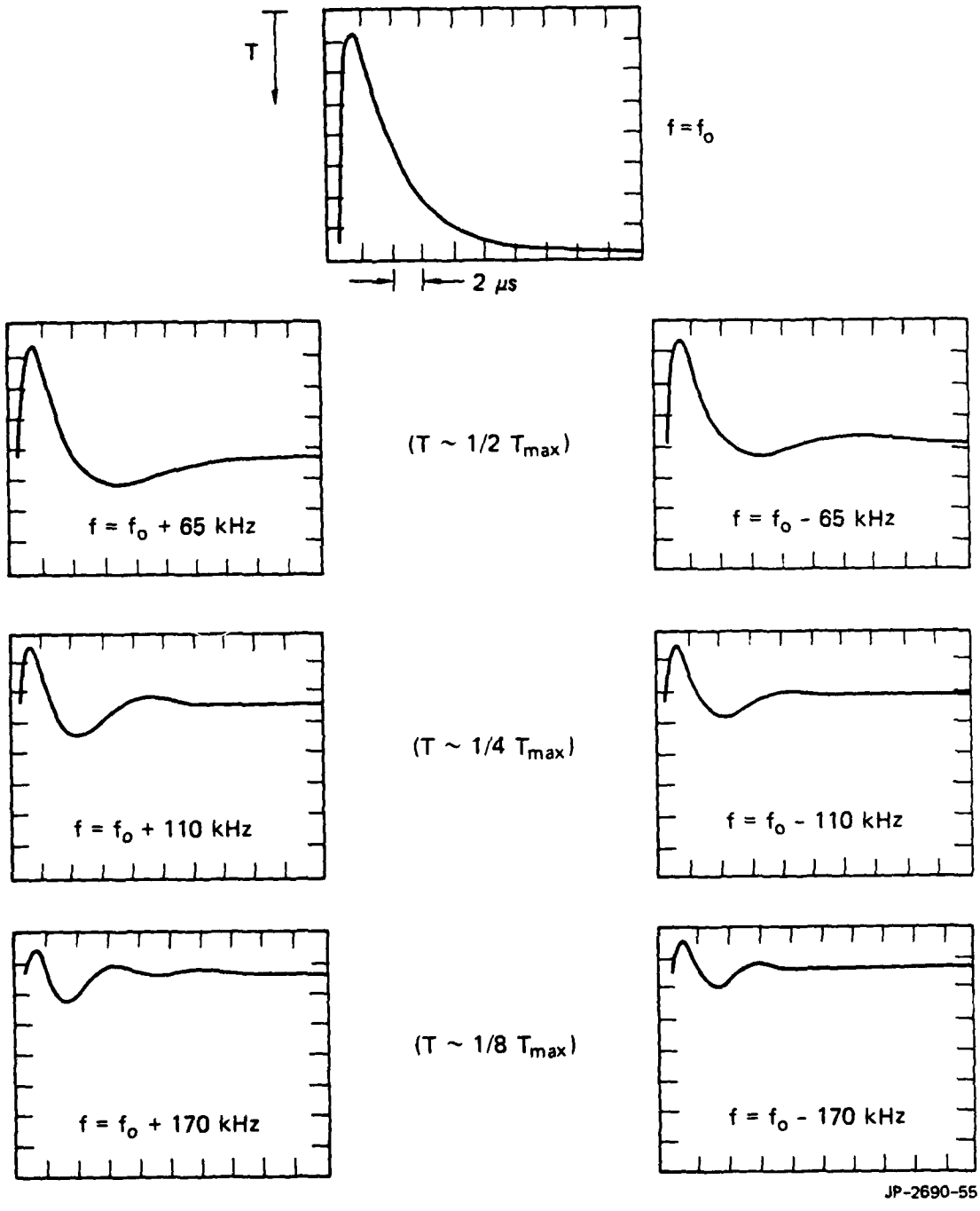

FIGURE 11 CAVITY TRANSMISSION HISTORIES FOR 1 amagat HUMID AIR
(Plasma diameter 2.65 cm, cavity bandwidth ~ 140 kHz, f_o = 1.507 GHz)

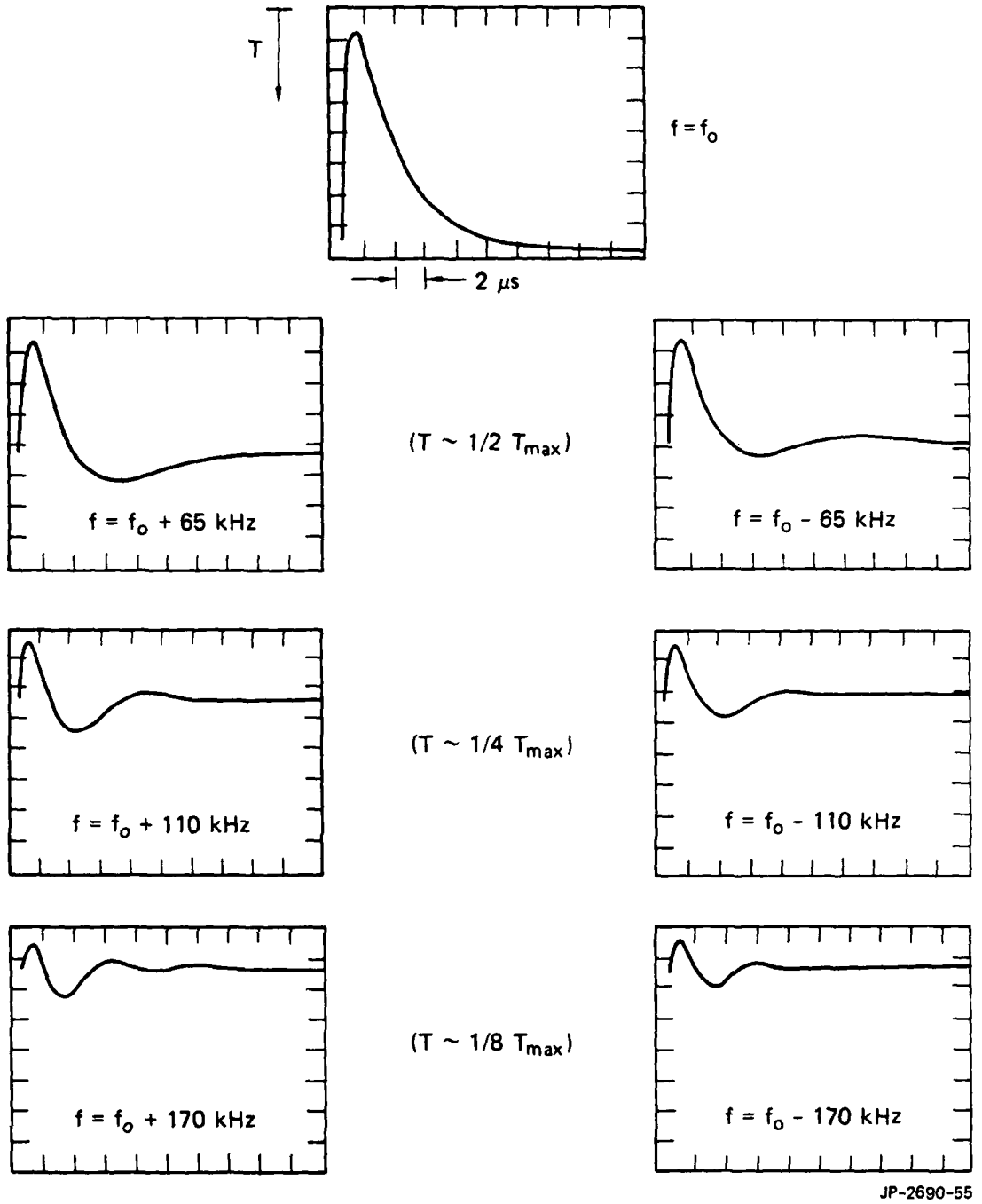

FIGURE 11 CAVITY TRANSMISSION HISTORIES FOR 1 amagat HUMID AIR
(Plasma diameter 2.65 cm, cavity bandwidth ~ 140 kHz, f_o = 1.507 GHz)

If one reads transmissions at equal time intervals on each trace and crossplots to obtain $T = T(f)$ at specific ts, a plot like Figure 12 is obtained. Neglecting the effects of ringing, we can determine three parameters for each curve: $T_{max}(t)$, $\frac{f}{\Delta f}(t)$, and, at least approximately, $\Delta f_{shift}(t)$. The first two parameters offer alternative ways of determining $\Delta(\frac{1}{Q})(t)$ from equations (3.14) and from the definition $Q = f/\Delta f$. Determining $\Delta(\frac{1}{Q})(t)$ by the two methods gives two sets of $\sigma_r(t)$, as shown in Figure 13. The two sets of results are in good agreement, with the results based on (T_c'/T_c) considered more reliable. Likewise, $\Delta f_{shift}(t)$ can be used to determine $\sigma_i(t)$, as shown in Figure 14.

If one assumes that these conductivities are due to electrons, and assigns a temperature (or collision frequency) to them, one can use equation (3.7), Table 1, and Figure 1 to calculate the electron densities that would cause the σ_rs and σ_is of Figures 13 and 14. If this is done, the n_es determined from σ_i are about 10 times higher than those from σ_r ($4 \times 10^{10}/cm^3$ at 1 μs, compared with $3 \times 10^9/cm^3$). Clearly, something is amiss, most likely the assumption that the conductivities are due to electrons.

Instead of assuming a collision frequency, one can determine the actual value of ν from the ratio of perturbations (in the ν = constant approximation)

$$\nu = \frac{\omega}{2} \frac{\Delta(\frac{1}{Q})}{(\frac{\Delta f}{f})_{max}} \quad . \tag{4.1}$$

Results obtained using the average $\Delta(\frac{1}{Q})$ and $\Delta f/f$ are presented in Figure 15 (division by ρ = amagats does not affect these 1-amagat data).

It should be emphasized that the analysis to this point has not required knowing the identity(s) of the charged particles. The conductivities of Figures 13 and 14 are correct, as are the νs of Figure 15. If we assume that they are electrons, we can calculate $n_e(t)$ as shown in Figure 16. The results from the three data sources are now in good agreement, as indeed they must be since the experimental ν was used in the calculations.

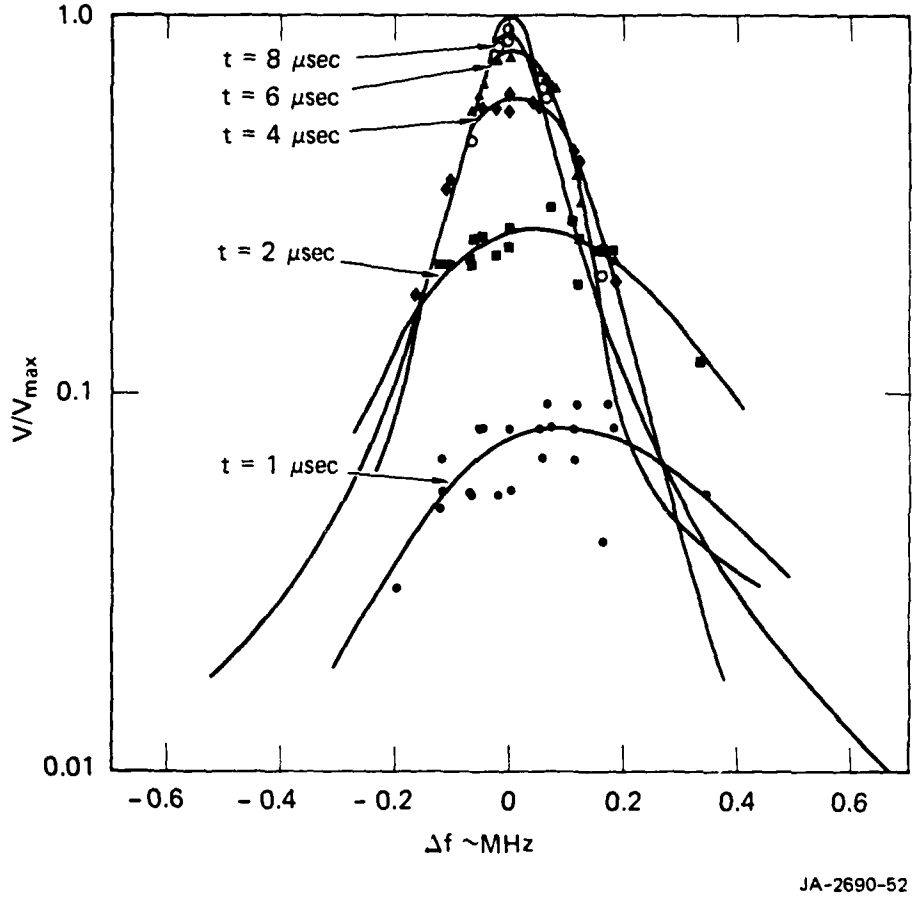

FIGURE 12 TRANSMISSION PROFILES IN HUMID AIR AT 1 amagat

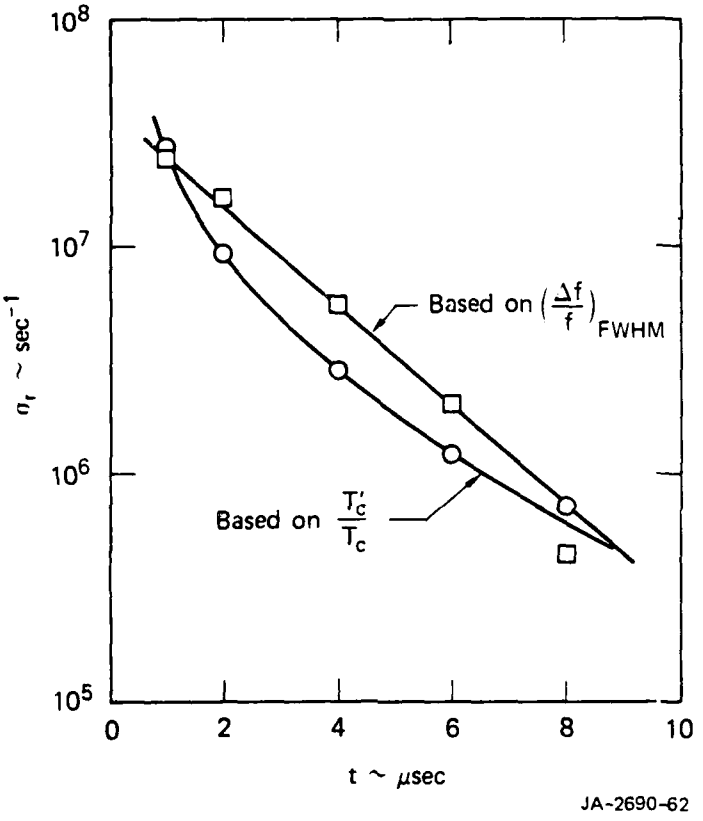

FIGURE 13 REAL CONDUCTIVITY HISTORIES FOR 1 amagat HUMID AIR (R_p = 1.3 cm)

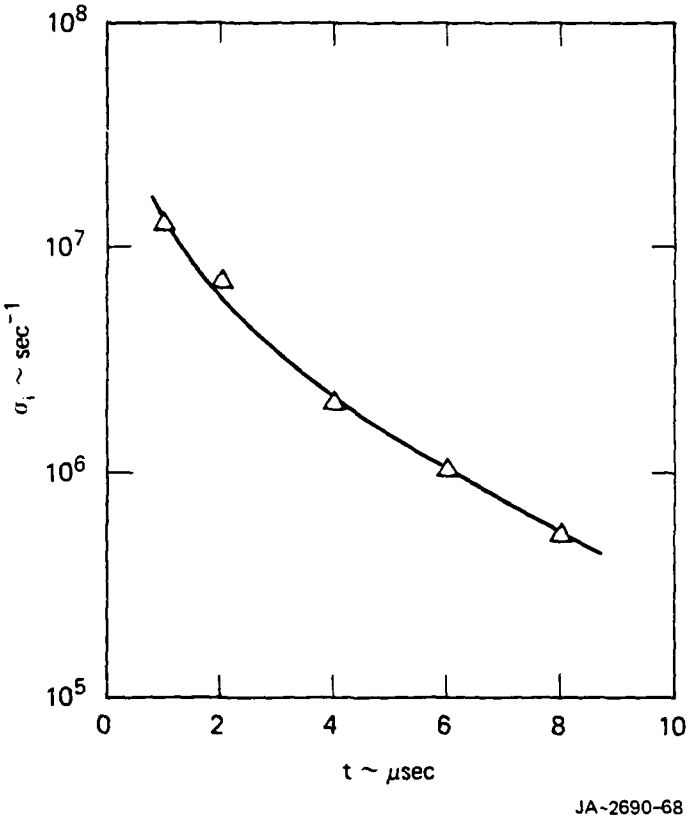

FIGURE 14 IMAGINARY CONDUCTIVITY HISTORY FOR 1 amagat HUMID AIR (R_p = 1.3 cm)

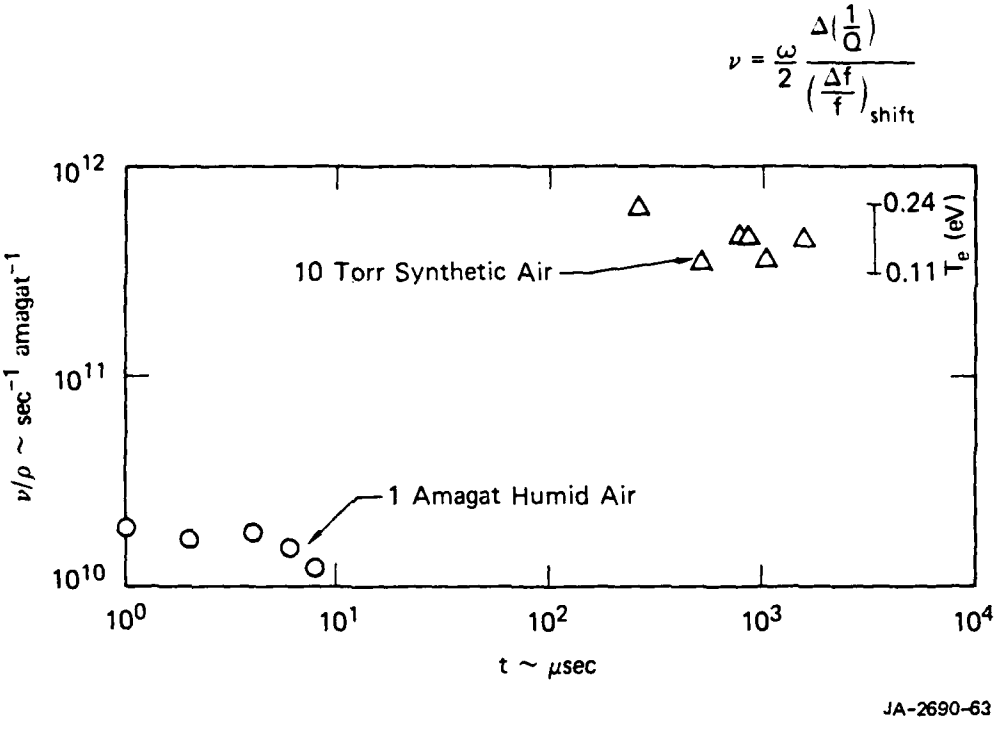

FIGURE 15 COLLISION FREQUENCIES DEDUCED FOR CHARGED PARTICLES IN AIR AFTERGLOWS

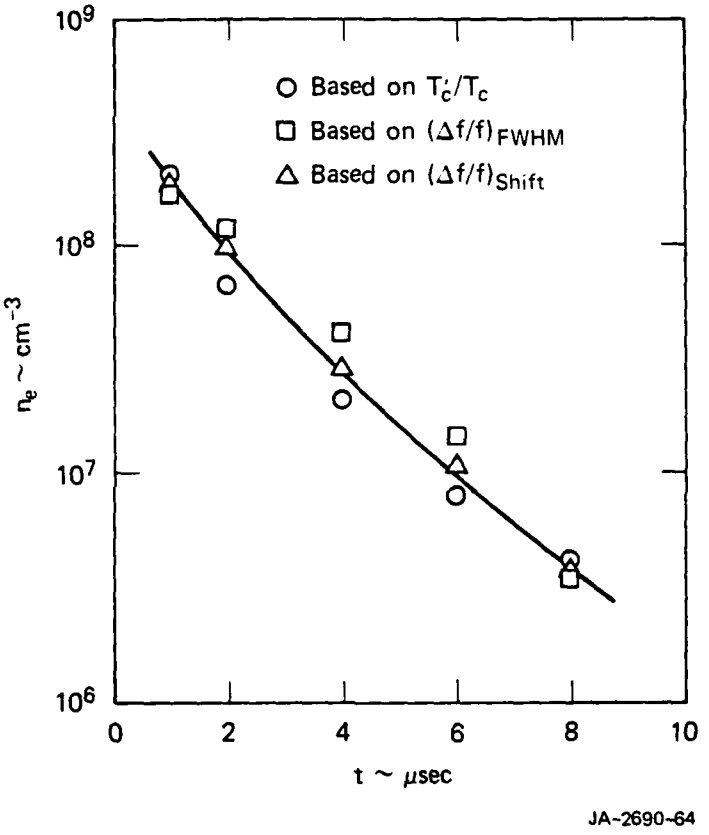

FIGURE 16 DEDUCED ELECTRON DENSITY HISTORIES FOR 1 amagat HUMID AIR

It is unlikely that electrons are the charge carrier in these measurements for two reasons. First, a comparison of the νs from Figure 15 with the calculated values shown in Figure 1 shows that the measured values are more than 10 times smaller than the calculated values for humid air. Second, the attachment rate of electrons to O_2 in air at 1 amagat is very fast,

$$\frac{dn_e}{dt} = -\beta n_e N^2 = -\beta' n_e \quad , \tag{4.2}$$

where $\beta' = 8 \times 10^7\ \rho^2\ s^{-1}$ for room temperature electrons. This attachment rate should reduce the electron density below $10^4/cm^3$ by 300 ns, whereas Figure 16 indicates $n_e = 10^8/cm^3$ at 2 μs. The microwave fields in the cavity might heat the electrons and slow down attachment somewhat, but not enough to account for such differences.

The other identification of charged particles is ions, now viewed as positive/negative ion pairs. Ion conductivities are usually neglected because when $n_e \approx N_i$,

$$\left(\frac{\omega_{pe}}{\omega_{pi}}\right)^2 = \frac{m_i}{m_e} > 5.8 \times 10^4 \qquad \text{(for } O_2^-\text{)} \tag{4.3}$$

(where m is the mass) so that electrons dominate the imaginary conductivity, and the mobility ratios for electrons and ions are

$$\frac{\mu_e}{\mu_i} \approx 10^4 \tag{4.4}$$

so that again electrons dominate the real conductivity. This neglect of ions is no longer valid when $n_i >> 10^4\ n_e$.

If we assign the conductivity to ions, then with an assumption about m_i, we can calculate n_i since we have already determined ν experimentally. Let us assume, for example, that the dominant negative ion is O_4^- and the dominant positive ion is $H_3O^+ \cdot H_2O$. Then the effective mass (in atomic units) is

$$\bar{m}_{eff} = \frac{m_1 m_2}{m_1 + m_2} = \frac{64 \times 37}{64 + 37} = 23 \quad . \tag{4.5}$$

The plasma frequency, $\omega_p = 2\pi f_p$, is then related to the ion density by

$$\omega_{pi} = \left(\frac{n_i e^2}{\bar{m}_{eff} \varepsilon_o}\right)^{1/2} = 7.6 \times 10^4 \, n_i^{1/2} \tag{4.6}$$

We can then use the ν = constant expression for either σ_r or σ_i from Table 1 to calculate ω_p and consequently n_i from the results of Figure 13 or 14. The resulting ion density history is presented in Figure 17. The ion densities are 4×10^4 times larger than the electron densities of Figure 16; this is just the ratio $\bar{m}_{eff}/m_e$.

The collision frequency, ν, is related to the collisional cross section, σ_c, and the drift velocity, v_D, by the relationship

$$\nu = n\sigma_c v_D \quad . \tag{4.7}$$

If we approximate v_D by the average ion velocity

$$v_D \simeq \bar{v} \, (8kT/\pi\bar{m}_{eff})^{1/2} \quad , \tag{4.8}$$

which is $\bar{v} \simeq 5 \times 10^4$ cm/s, we find that $\sigma_c \simeq 1.3 \times 10^{-14}$ cm^2. This is only somewhat larger than a typical ion collision cross section of $\sigma_c \simeq 5 \times 10^{-15}$ cm^2 [McD64], perhaps reflecting the fact that v_D is larger than $\bar{v}$. The collision frequency can also be related to the ion mobility K by

$$K = \frac{e}{\bar{m}_{eff} \varepsilon_o} \frac{\nu}{\omega^2 + \nu^2} \quad . \tag{4.9}$$

This yields K $\simeq$ 2.0 cm^2/V-s, which is in excellent agreement with typical values for ions at low electric fields [McD64]. Both these calculations support the assignment of the measured conductivity to ions for this 1 amagat humid air case.

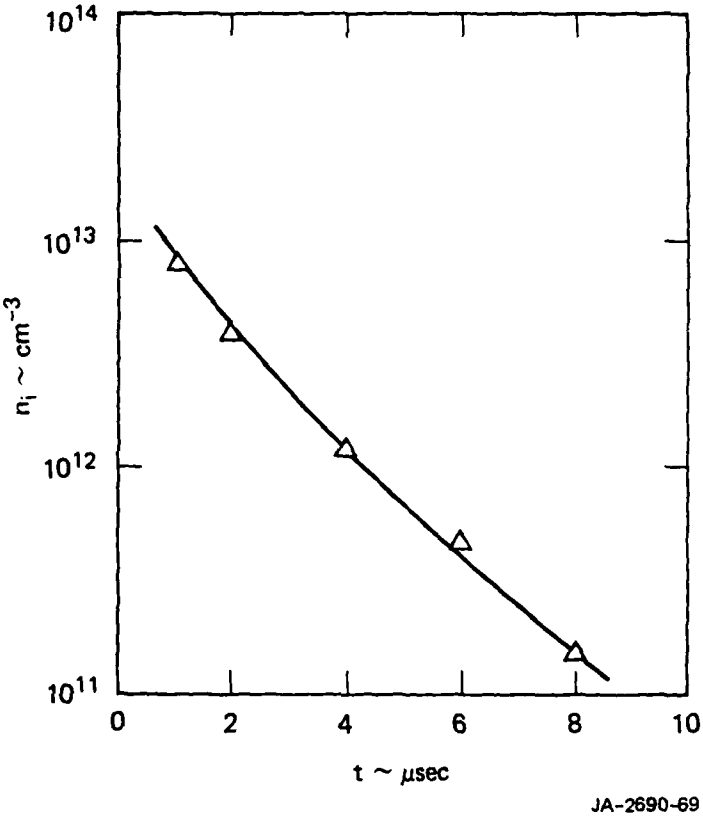

FIGURE 17 DEDUCED ION DENSITY HISTORY FOR 1 amagat HUMID AIR

(Assume $\bar{m}_{eff}$ = 23 amu)

For 10-torr synthetic air, the situation seems much more straightforward. Representative scope traces of cavity transmission at f_o and three $\pm\Delta$fs are shown in Figure 18; there are three marked differences from the 760 torr data of Figure 12. First, the time scale for plasma decay is about 250 times as long. Second, the + and - Δf curves are now unsymmetric because the frequency shift is larger than the broadening due to $\Delta(\frac{1}{Q})$, as expected from Figures 6 and 7. Third, the superimposed ringing is no longer present. Crossplotted signal histories at 250 μs intervals are presented in Figure 19. Again, we can determine σ_r from $\frac{T_c}{T_c}(t)$ or from $(\frac{f_o}{\Delta f})(t)$, with the results shown in Figure 20. Again, the two techniques give good agreement. If we now calculate ν from equation (3.22) and normalize the results to 1 amagat, we obtain the results also shown in Figure 15. These collision frequencies are consistent with the dry air results of Figure 1 at approximately 0.15 eV ($\simeq$ 1700 K). The electrons are probably in equilibrium with the vibrational mode of N_2 at this temperature. It is less likely that the elevated T_e is due to the microwave field heating the electrons, but that effect should be checked by varying the source power.

The electron density histories deduced from σ_r, σ_i, and ν are presented in Figure 21. Presumably, the decay is due to attachment, which finally takes over when the densities drop too low for recombination to dominate. Such a decay would be exponential (linear on Figure 21). The best linear fit to the data gives $\beta' \simeq 2 \times 10^7\ \rho^2\ s^{-1}$, compared with a value for room temperature electrons of $\beta' \simeq 8 \times 10^7\ \rho^2\ s^{-1}$. A higher electron temperature of $\simeq$ 0.15 eV deduced from the ν's of Figure 15 would be expected to increase the attachment rate by a factor of 4 [CPB62], in contrast with the reduction observed in the present results. The reduction and the nonexponential electron decay may be due to detachment of electrons from negative ions by collision with excited species, which could include N_2 (vib), $N_2(A)$, $O_2(^1\Delta)$, and $O_2(^1\Sigma)$.

Pressure Scans

The results reported above involved 15 to 20 tests in each case, with the attendant amount of data reduction. It was not appropriate to repeat this lengthy procedure for preliminary tests at many pressures, but we did make several measurements at f_o only over a wide pressure range. These results can

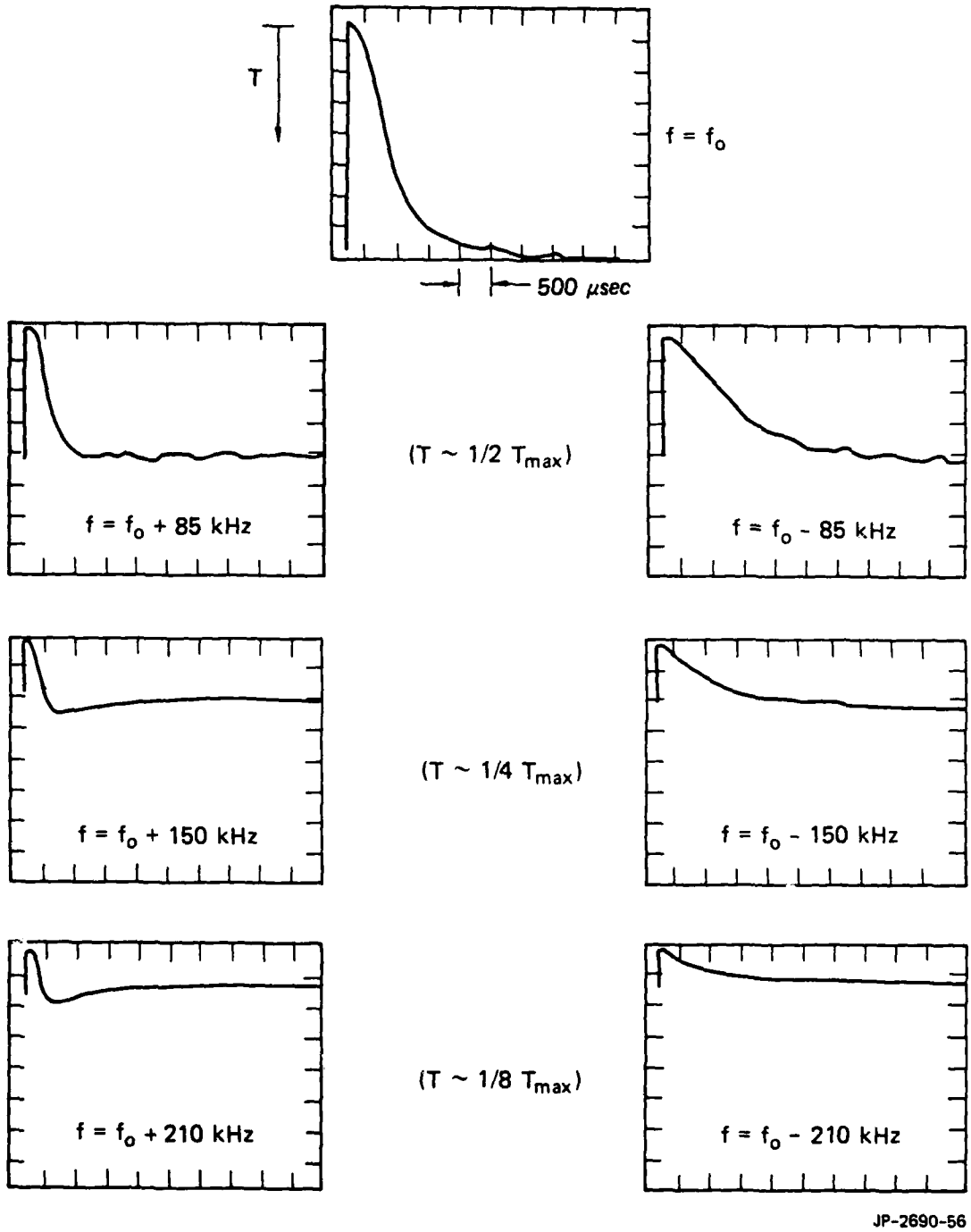

FIGURE 18 CAVITY TRANSMISSION HISTORIES FOR 10 TORR SYNTHETIC AIR
(Plasma diameter 2.65 cm, cavity bandwidth ~ 140 kHz, f_o = 1.507 GHz)

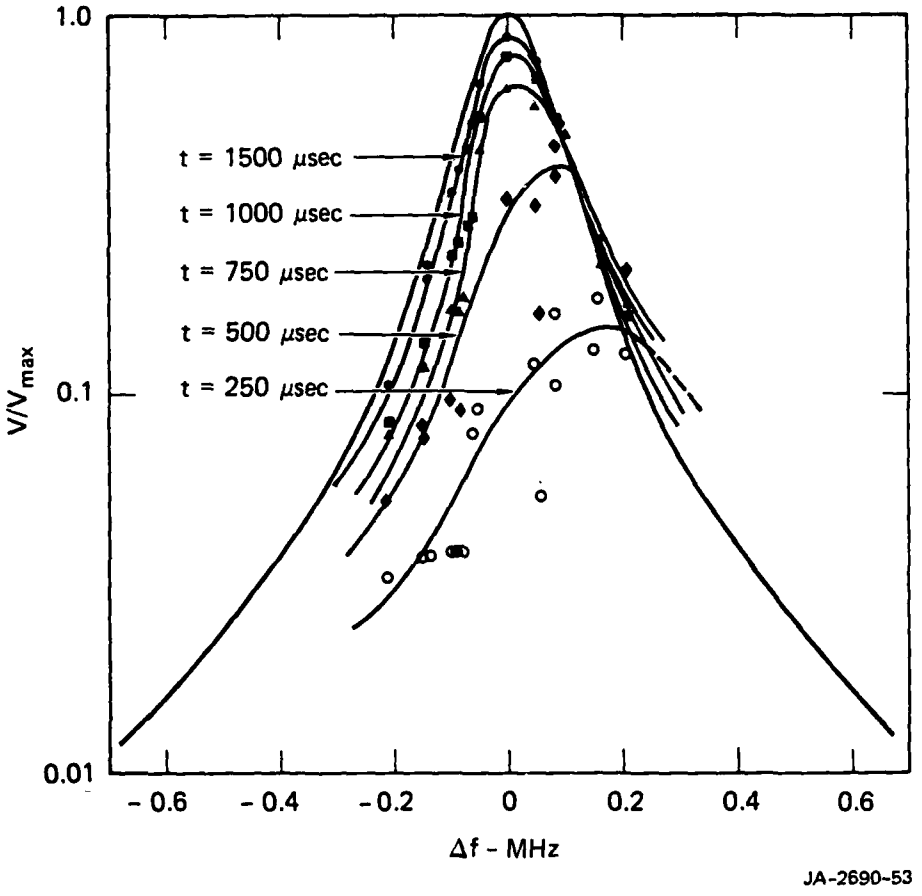

FIGURE 19 TRANSMISSION PROFILES IN SYNTHETIC AIR AT 10 torr

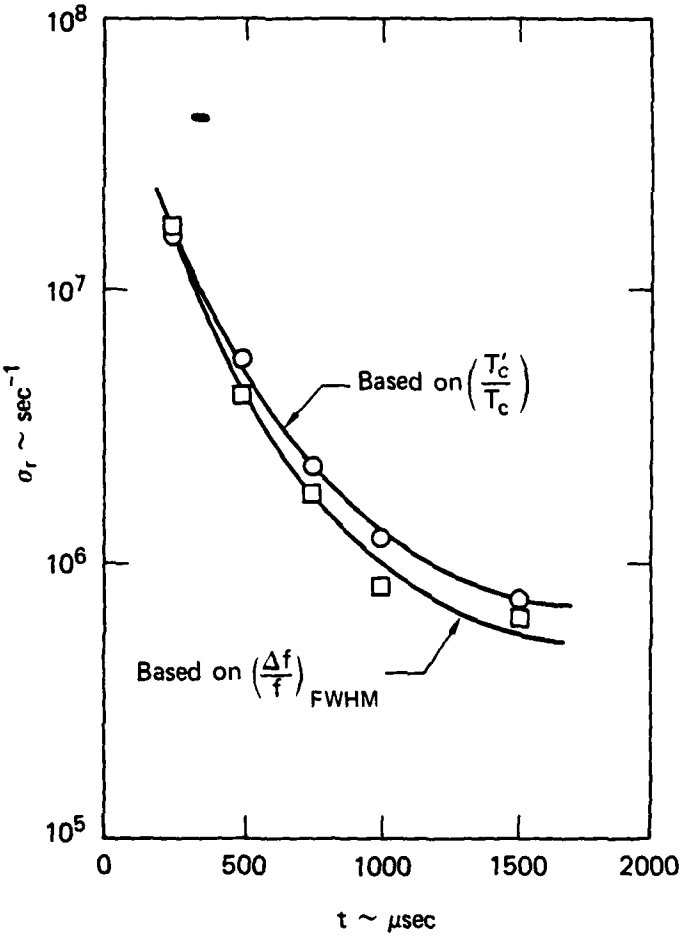

FIGURE 20 REAL CONDUCTIVITY HISTORIES FOR 10 torr SYNTHETIC AIR

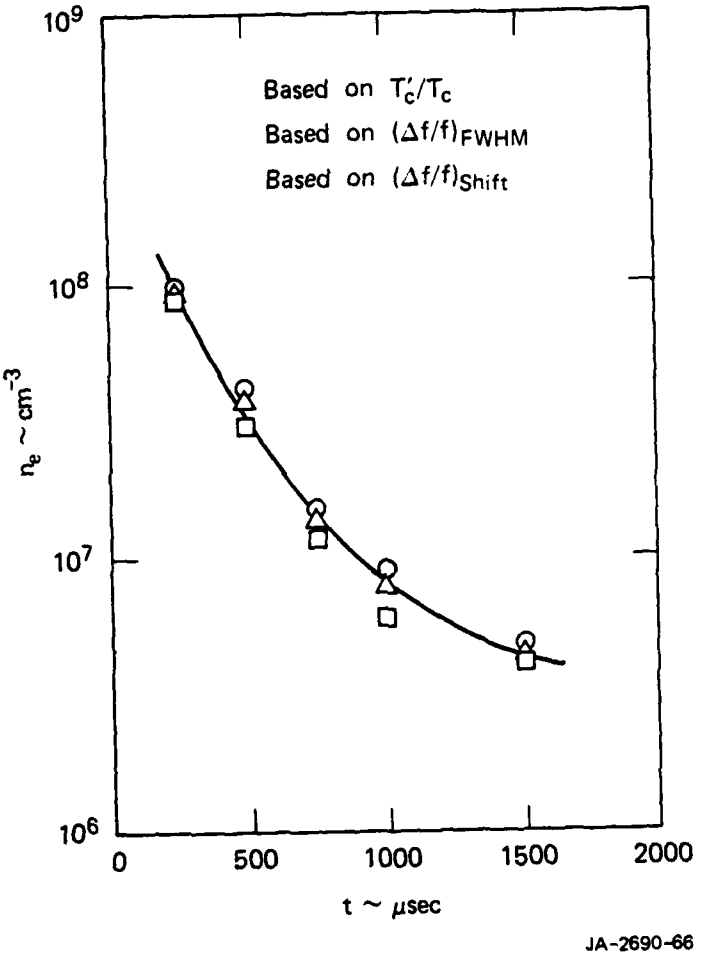

FIGURE 21 ELECTRON DENSITY HISTORIES FOR 10 torr SYNTHETIC AIR

be used to determine σ_r by the (T_c'/T_c) method if we neglect the fact that part of the reduction of transmission at $f \approx f_o$ results from a frequency shift rather than a $\Delta(1/Q)$ broadening. This approximation will cause the most severe errors in low pressure and early time results.

Transmission histories for two series of tests that compare the results of laboratory and synthetic air are presented in Figure 22. Except for the $p = 760$ torr results, the conductivity decays are always significantly longer in synthetic air than in laboratory air. It is known that H_2O is a much more effective third body in attachment of electrons to O_2, and the results of Figure 22 can be explained if the partial pressure of H_2O stayed constant as the total pressure was reduced. We also find that the decay times in synthetic air rapidly decrease with impurity level, causing considerable scatter in these preliminary results.

The conductivity decays get progressively longer with decreasing pressure, until at 3 torr in synthetic air and 1 torr in laboratory air, the character of the decay changes markedly. We assume that these are the pressures where diffusion of electrons to the walls becomes faster than attachment. These rather low pressures then mark the lower limits of these measurements in air.

We pointed out above that we can determine $\sigma_r(t)$ from these traces if we neglect the contribution of frequency shifts to reduction of transmission. This neglect would tend to make the σ_r values low at the beginning of each trace, particularly at lower pressures. Results for two series of tests in synthetic air, one with a quartz tube of 26.5-mm ID lining the cavity and the second using a 20-mm-ID tube, are presented in Figures 23 and 24. The purpose of the two series was to look for a possible wall effect on the measurements. The two sets of results are similar but not identical, and the accuracy of these preliminary data is not good enough to warrant a firm conclusion. A third series of tests with no tube at all showed quite similar conductivity decay times, but since we do not know the plasma area in that case, we cannot calculate the σ_rs.

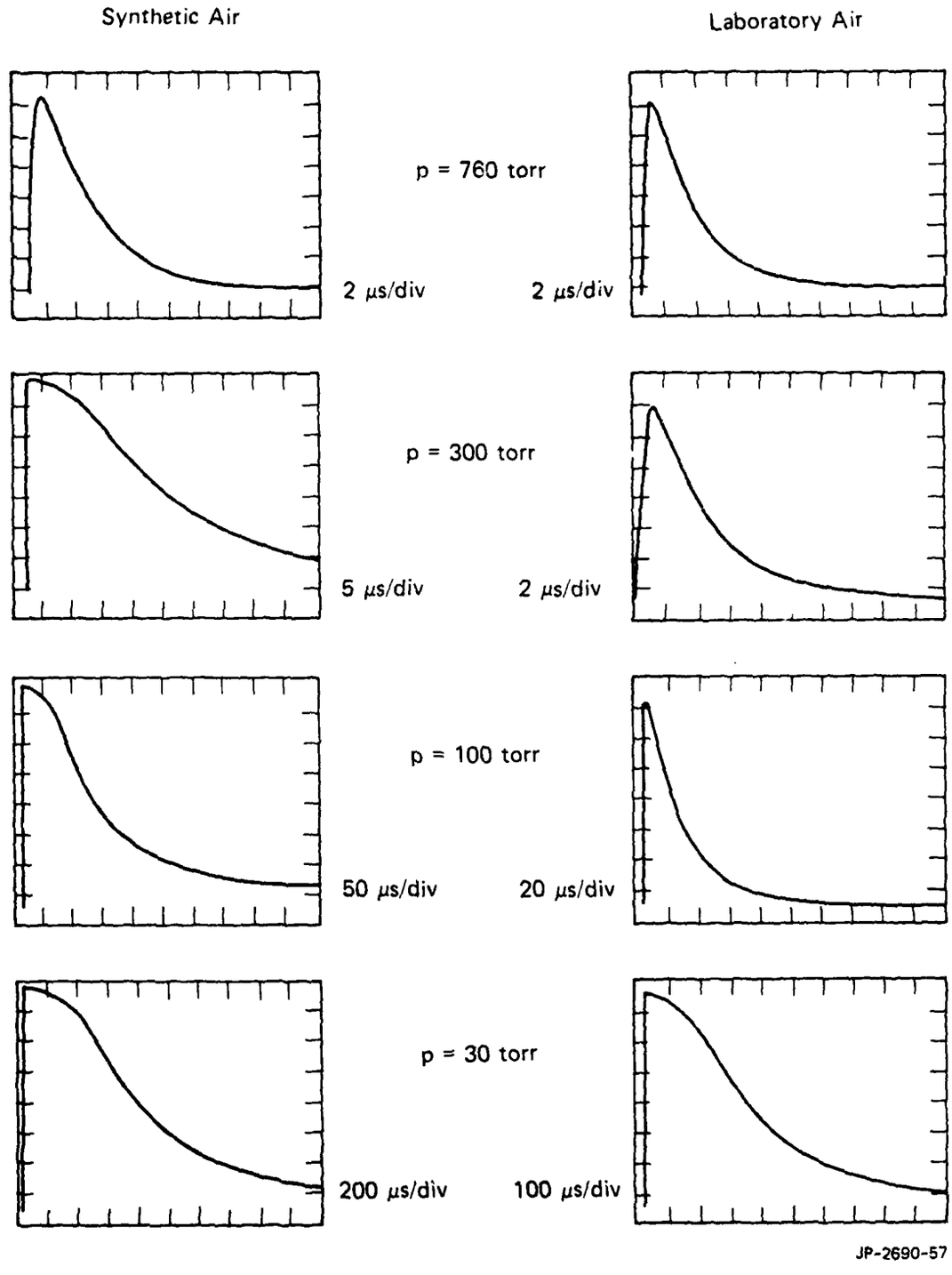

FIGURE 22 CAVITY TRANSMISSION HISTORIES FOR SYNTHETIC AND LABORATORY AIR

($f = f_o = 1.537$ GHz, plasma diameter = 2.0 cm, cavity bandwidth ~ 160 kHz)

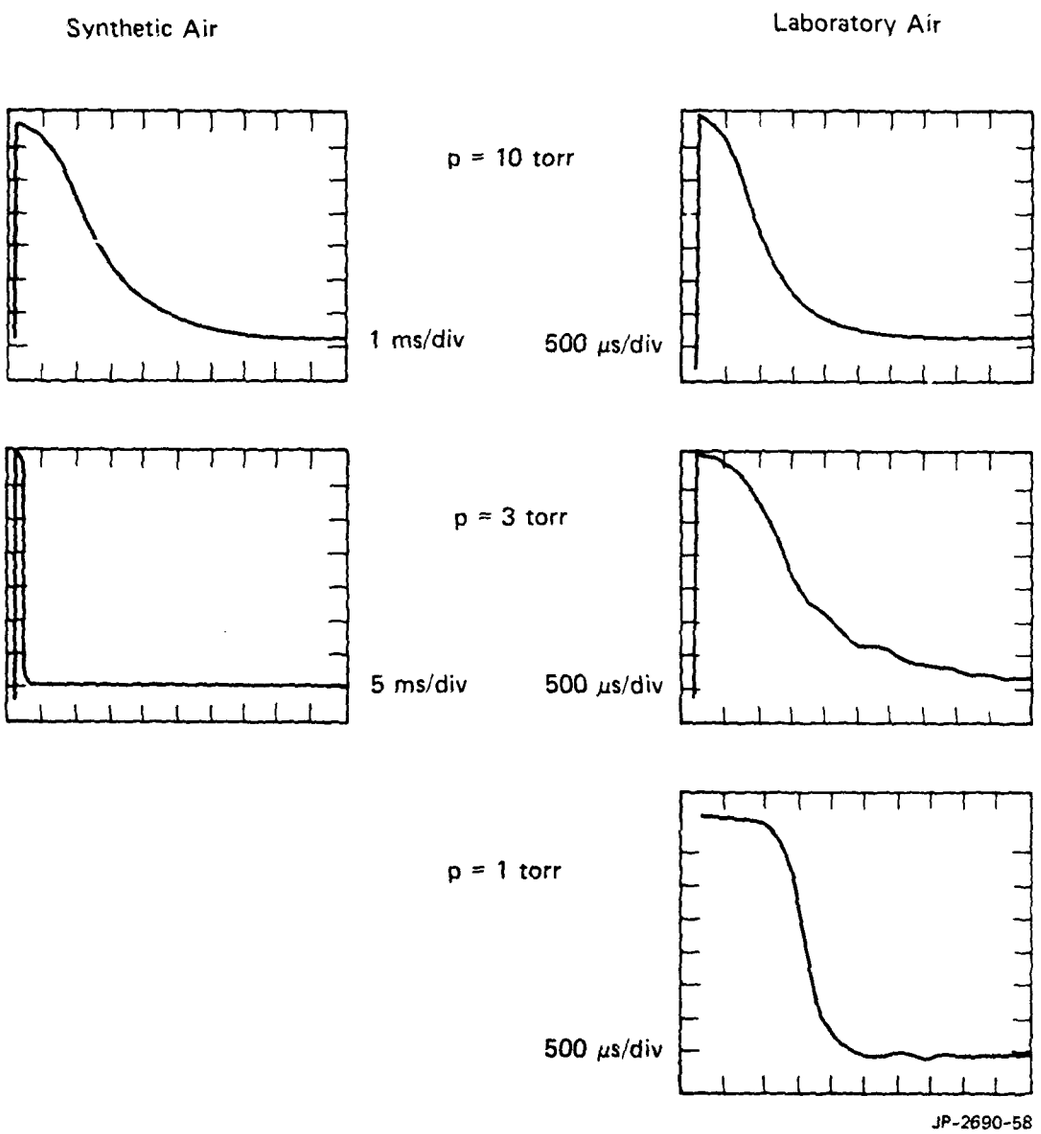

FIGURE 22 CAVITY TRANSMISSION HISTORIES (Concluded)

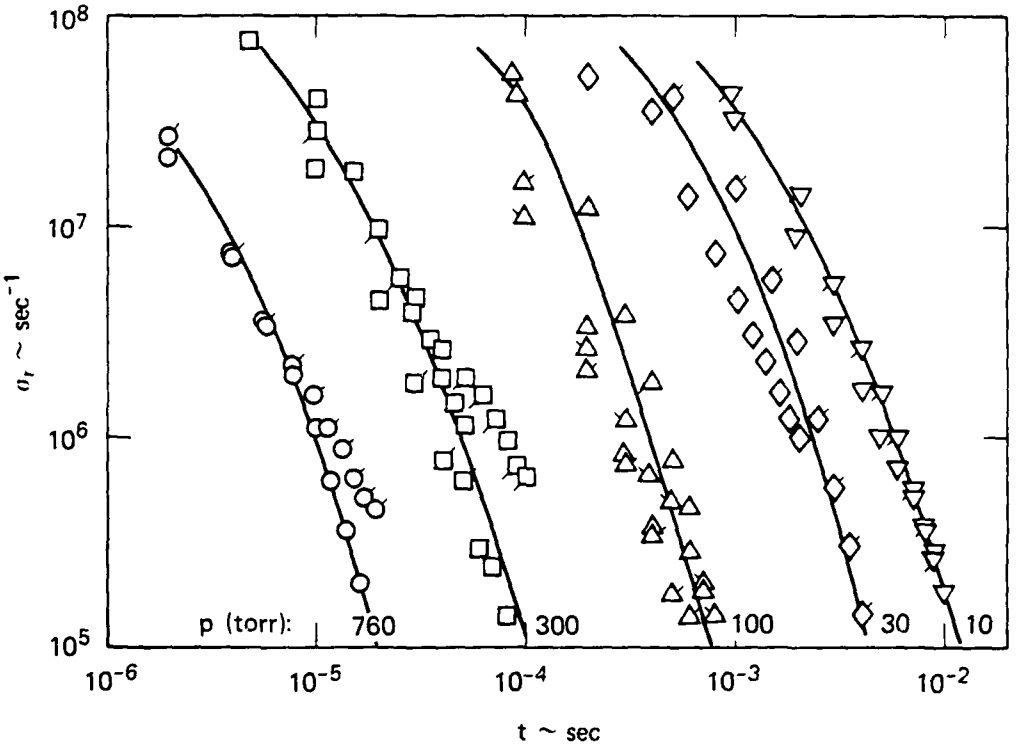

FIGURE 23 CONDUCTIVITY HISTORIES IN SYNTHETIC AIR FOR VARIOUS PRESSURES
(f_o = 1.507 GHz, Plasma Diameter = 2.65 cm)

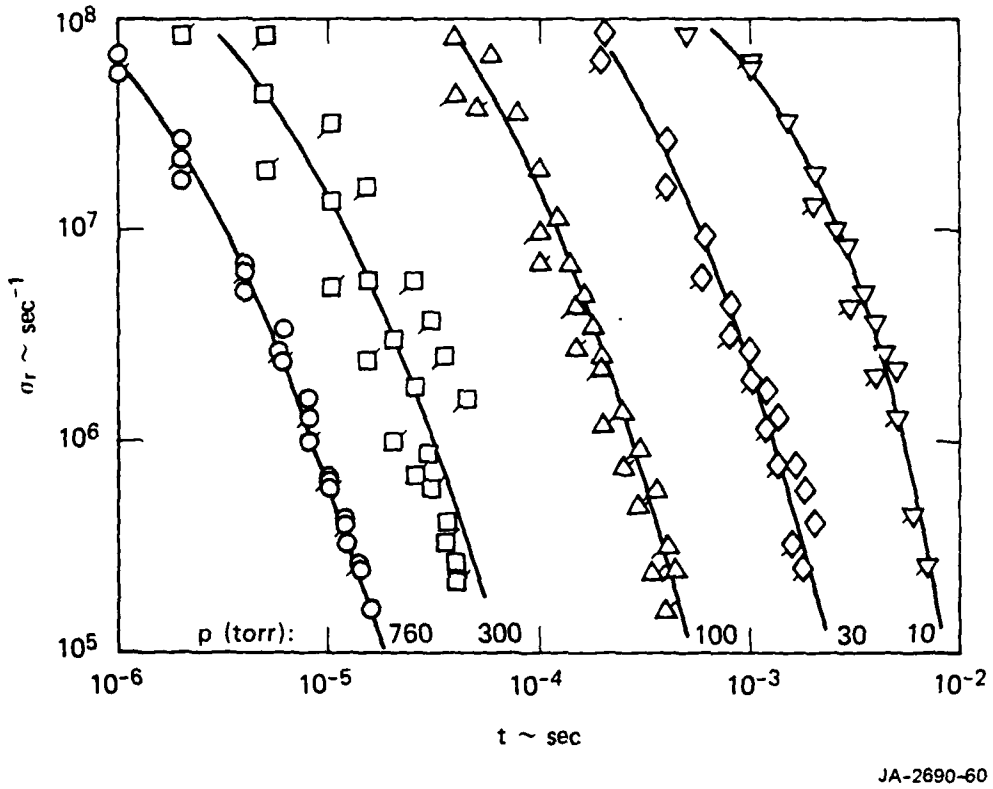

FIGURE 24 CONDUCTIVITY HISTORIES IN SYNTHETIC AIR FOR VARIOUS PRESSURES (f_o = 1.537 GHz, Plasma Diameter = 2.0 cm)

V CONCLUSIONS AND PLANS

The work reported here indicates that the microwave cavity perturbation technique will be a powerful tool for diagnosing the afterglow channel of high energy electron beams. The most sensitive measurement is of the real conductivity (which is the D.C. conductivity at high pressures). We have demonstrated detectivity limits of $\sigma_r \gtrsim 10^5\ s^{-1}$ for a 2.65-cm-diameter plasmas; the sensitivity varies inversely with plasma diameter, so that the threshold for a 1-cm-diameter plasma is $\sigma_r \gtrsim 10^6\ s^{-1}$. This is, in fact, somewhat more sensitive than desired for diagnosing ETA or ATA experiments, but the sensitivity can easily be reduced (most readily by increasing the coupling of the input and output loops). Thus far, our sensitivity limit for the imaginary conductivity has been about the same as that of the real conductivity, or $\sigma_i \gtrsim 5 \times 10^5\ s^{-1}$ (again for a 2.65-cm-diameter plasma).

Either the real or imaginary conductivities can be used to deduce electron densities if a collision frequency is assumed. Alternately, the ratio of conductivities gives the collision frequency directly, and the electron densities can then be calculated. Furthermore, comparing the measured collision frequencies with calculated values allows one to deduce electron temperatures. Since electron energies are often equilibrated with vibrational energies, this indicates vibrational temperatures as well. Thus, the technique offers determination of a wide range of information.

When attachment dominates over recombination in the early afterglow, negative ion densities can become several orders of magnitude larger than electron densities. Then, the conductivity is due to ions rather than electrons. In our measurements to date, this effect manifested itself when collision frequencies were inconsistent with values expected for electrons. The conductivity measurement remains valid even in this case. Furthermore, application of pulsed fields in the cavity (microwave or D.C.) to detach bound electrons from ions might simulate the fields induced by a high current electron beam, and furnish information on the change in residual conductivity that occurs in the nose of a second or subsequent pulse.

There are many refinements to be made to the system before taking final data. First, a much more stable microwave source is needed so that recordings can be taken at fixed and known frequencies (this source is currently being procured). A high purity vacuum system is needed to take data with synthetic air because the preliminary results showed that the conductivity was sensitive to impurities (presumably water vapor). It would be helpful to add a magnetic field to the cavity to confine the Febetron electron beam to a more nearly cylindrical geometry. With or without the field, the beam axial current profile should be mapped with a Faraday cup probe and/or open shutter photography. Finally, the effect of microwave power level on the afterflow decay should be investigated.

These refinements will lead to measurements using our Febetron 706 electron beam source that should provide definitive conductivity histories for room temperature air as a function of pressure. The experiment is also designed to fit directly onto the ETA facility for similar measurements on that beam. This will be particularly interesting when ETA is operated in the burst pulse mode. Future work will also include extending the measurements to high temperature (shock-heated) air to investigate the effects of temperature on conductivity decay.

REFERENCES

BF49 G. Birnbaum and J. Franeau, J. Appl. Phys. 20, 817 (1949).

CPB62 L. M. Chanin, A. V. Phelps, and M. A. Biondi, Phys. Rev. 128, 219 (1962).

DK75 G. Dodel and W. Kunz, Appl. Optics 14, 2537 (1975).

GF71 V. M. Ginzburg and Yu. I. Filenko, Soviet Phys. -Tech. Phys. 15, 1730 (1971).

Ha63 A. F. Harvey, Microwave Engineering, Academic Press, London, 1963.

HW65 M. A. Heald and C. B. Wharton, Plasma Diagnostics With Microwaves, John Wiley and Sons, New York (1965).

It71 Y. Itikawa, Planet. Space Sci. 19, 993 (1971).

It73 Y. Itikawa, Phys. Fluids 16, 831 (1973).

KW64 G. D. Kahl and E. H. Wedemeyer, Phys. Fluids 7, 596 (1964).

Lu68 P. Lukac, J. Phys. D, Series 2 1, 1495 (1968).

McD64 E. W. McDaniel, Collision Phenomena In Ionized Gases, John Wiley and Sons, New York, 1964.

Mo47 C. G. Montgomery, Technique of Microwave Measurements, McGraw-Hill Book Company, Inc., New York, 1947.

Sh61 J. Shmoys, J. Appl. Phys. 32, 689 (1961).

Sl46 J. C. Slater, Rev. Modern Phys. 18, 441 (1946).

SL46 R. L. Sproull and E. G. Linder, Proc. I.R.E. 34, 305 (1946).

Th63 K. I. Thomassen, J. Appl. Phys. 34, 1622 (1963).

Th65 K. I. Thomassen, J. Appl. Phys. 36, 3642 (1965).

Ver79 D. Veron, in Infrared and Millimeter Waves. Vol. 2 Instrumentation, Edited by K. J. Button, Academic Press, New York, 1979.

Ves75 C. M. Vest, Appl. Optics 14, 1601 (1975).